NEBRASKA
Good Life. Great Journey.
DEPARTMENT OF TRANSPORTATION

Report SPR-P1(17) M075

Development and Implementation of a Moving Nondestructive Evaluation Platform for Bridge Deck Inspection

Sepehr Pashoutani, Jinying Zhu, Chungwook Sim
Department of Civil Engineering, University of Nebraska-Lincoln

Brian Mazzeo, Spencer Guthrie
Brigham Young University

April 2020

TECHNICAL REPORT DOCUMENTATION PAGE

1. Report No. M075	2. Government Accession No.	3. Recipient's Catalog No.
4. Title and Subtitle Development and Implementation of a Moving Nondestructive Evaluation Platform for Bridge Deck Inspection		**5. Report Date** April 2020 **6. Performing Organization Code**
7. Author(s) Sepehr Pashoutani, Jinying Zhu, Brian Mazzeo, Spencer Guthrie, Chungwook Sim		**8. Performing Organization Report No.**
9. Performing Organization Name and Address Department of Civil and Environmental Engineering. University of Nebraska-Lincoln 1110 S 67th St., Omaha, NE 68182		**10. Work Unit No.** **11. Contract** SPR-P1(17) (M075)
12. Sponsoring Agency Name and Address Nebraska Department of Transportation Research Section 1400 Hwy 2 Lincoln, NE 68502		**13. Type of Report and Period Covered** Final Report July 2017 – April 2020 **14. Sponsoring Agency Code**
15. Supplementary Notes		

16. Abstract

Degradation in concrete bridge decks is typically manifested as rebar corrosion, concrete delamination, and surface cracks. Nondestructive evaluation and testing (NDE/NDT) technologies have been increasingly used in concrete bridge deck evaluation to identify, localize, and quantify deterioration in bridge decks. Each NDE method has its advantages and limitations on the type of defect that can be detected. Therefore, combining multiple NDE technologies is needed in order to give comprehensive and reliable information about the bridge deck condition. For effective application of multiple NDE tests, we need to use automated positioning for each NDE to facilitate post-processing and data fusion of different NDE data.

In this research work, the research team developed an NDE platform that will allow multiple NDE data collections either simultaneously or in sequence, with real time position information on bridge decks. The NDE platform consists of two main components: the data collection unit and the localization box. The data collection unit is made of a series of single board computers that were linked together to acquire data from many different channels. Any NDE technology with open data connection can be connected to the platform. The localization box incorporates localization devices including LiDAR, DGPS, and a camera as distance measurement instrument to accurately locate the signals captured by data collection unit. The moving NDE platform can be attached to hitch extension of a vehicle to provide a completely mobile solution.

Three Nebraska bridges were surveyed using four NDE technologies: Vertical Electrical Impedance (VEI), GPR, acoustic scanning system, and high definition imaging. Each bridge has different overlay type: no overlay, concrete overlay, and asphalt overlay. For each bridge deck, post-processed NDE data were analyzed, combined using two advance data fusion algorithms, and the final results are presented in 2D image maps.

17. Key Words	18. Distribution Statement
Nondestructive Evaluation (NDE), Platform, positioning, GPR, Vertical Impedance, Imaging, data fusion	No restrictions. This document is available through the National Technical Information Service. 5285 Port Royal Road Springfield, VA 22161

19. Security Classification (of this report)	20. Security Classification (of this page)	21. No. of Pages	22. Price
Unclassified	Unclassified	70	

DISCLAIMER

The contents of this report reflect the views of the authors, who are responsible for the facts and the accuracy of the information presented herein. The contents do not necessarily reflect the official views or policies neither of the Nebraska Department of Transportations nor the University of Nebraska-Lincoln. This report does not constitute a standard, specification, or regulation. Trade or manufacturers' names, which may appear in this report, are cited only because they are considered essential to the objectives of the report.

The United States (U.S.) government and the State of Nebraska do not endorse products or manufacturers. This material is based upon work supported by the Federal Highway Administration under SPR-1(17) (M075). Any opinions, findings and conclusions or recommendations expressed in this publication are those of the author(s) and do not necessarily reflect the views of the Federal Highway Administration."

Abstract

Degradation in concrete bridge decks is typically manifested as rebar corrosion, concrete delamination, and surface cracks. Nondestructive evaluation and testing (NDE/NDT) technologies have been increasingly used in concrete bridge deck evaluation to identify, localize, and quantify deterioration in bridge decks. Each NDE method has its advantages and limitations on the type of defect that can be detected. Therefore, combining multiple NDE technologies is needed in order to give comprehensive and reliable information about the bridge deck condition. For effective application of multiple NDE tests, we need to use automated positioning for each NDE to facilitate post-processing and data fusion of different NDE data.

In this research work, the research team developed an NDE platform that will allow multiple NDE data collections either simultaneously or in sequence, with real time position information on bridge decks. The NDE platform consists of two main components: the data collection unit and the localization box. The data collection unit is made of a series of single board computers that were linked together to acquire data from many different channels. Any NDE technology with open data connection can be connected to the platform. The localization box incorporates localization devices including LiDAR, DGPS, and a camera as distance measurement instrument to accurately locate the signals captured by data collection unit. The moving NDE platform can be attached to hitch extension of a vehicle to provide a completely mobile solution.

Three Nebraska bridges were surveyed using four NDE technologies: Vertical Electrical Impedance (VEI), GPR, acoustic scanning system, and high definition imaging. Each bridge has different overlay type: no overlay, concrete overlay, and asphalt overlay. For each bridge deck, post-processed NDE data were analyzed, combined using two advance data fusion algorithms, and the final results are presented in 2D image maps.

Acknowledgments

This research project would not have been possible without the funding provided by the Nebraska Department of Transportation. The authors would also like to acknowledge the engineers at the Department of Transportation for their assistance in this project, and especially Mark Traynowicz, Fouad Jaber, Jason Volz, Kent Miller for providing the bridge information and the arrangements of traffic controls in the field testing.

Contents

List of Figures

List of Tables

Chapter 1

Introduction

1.1 Background

The American Society of Civil Engineers (ASCE) periodically issues Report Card for America's Infrastructure. In 2017, the report card gave bridges a rate "C+". Among the 614,387 bridges in the National Bridge Inventory (NBI), 39% are over 50 years old. In Nebraska, 1,358, or 8.8 percent of the 15,349 bridges in the state, are classified as structurally deficient. This means one of the key elements - the deck, superstructure, substructure or culverts — is rated in poor or worse condition (ARTBA) [1]. Quantitative bridge evaluation may improve the public safety and help prioritize bridge repair spending.

The current practice of bridge inspection mainly relies on visual inspection, which may provide insufficient information for quantitative evaluation of concrete bridge deck conditions. Although many nondestructive evaluation (NDE) techniques have been developed for bridge deck evaluation [2–10], their application is still limited in practice. Possible challenges in NDE application may include: slow speed, complicated and expensive equipment, difficulties in interpreting NDE results to bridge engineers. FHWA sponsored development of an automated robotic NDE system, the RABIT [11], which integrates several NDE techniques in a single unit to automate multiple NDE scanning. However, this robotic system is expensive and requires extensive training and traffic control to operate. Individual NDE units may collect the data more efficiently than an integrated system when each unit has different scanning speed. The data from multiple NDE scans can be fused to achieve an reliable assessment when the positions of each scan are available.

This work outlines an approach that will make collecting NDE data significantly easier in the field and enable fusion of data through advanced post-processing algorithms. The

objective of this work was to construct a universal moving NDE platform that would provide spatial positioning information for multiple NDE modalities. Together with post-testing data fusion techniques, this platform allows layering data for visualization to bridge managers. It is anticipated that this platform will allow NDE data capture to aid bridge managers in making decisions about rehabilitation strategies for bridge decks.

An NDE platform is a tool used to collect data from any NDE techniques. An important aspect of various NDE platform is associating collected data with a spatial location on the structure. In its simplest form, the platform is a piece of paper on which an inspector writes the results of the evaluation technique. In more sophisticated forms, this platform gathers a wide variety of NDE data while simultaneously collecting positioning data to localize these measurements for future mapping.

State of the practice inspections are to have a human perform the evaluation and to record the test results on a piece of paper, or, in advanced cases, on an electronic device. This is illustrated in **Figure 1.1** and **Figure 1.2** for the example of chain dragging. An inspector drags a chain across the bridge deck and listens for a "hollow" resonance indicating delamination. When a delamination is detected, the outline of the delamination is marked on the bridge deck as shown in **Figure 1.1**. When the bridge deck has been chained, locations and extent of the delaminations are transcribed on paper as shown in **Figure 1.2**.

Fig. 1.1. State of the practice chain drag inspection on a bridge deck on which the locations of delaminations are marked using a handheld paint sprayer

In the manual chain drag test, data recording is slow and tedious. Examples of manual data recording can be found in the following research [6, 12]. Two common techniques to increase the data collection speed are wheel encoders and GPS solutions. A wheel encoder estimates the distance an NDE platform moves in a linear direction by counting the number

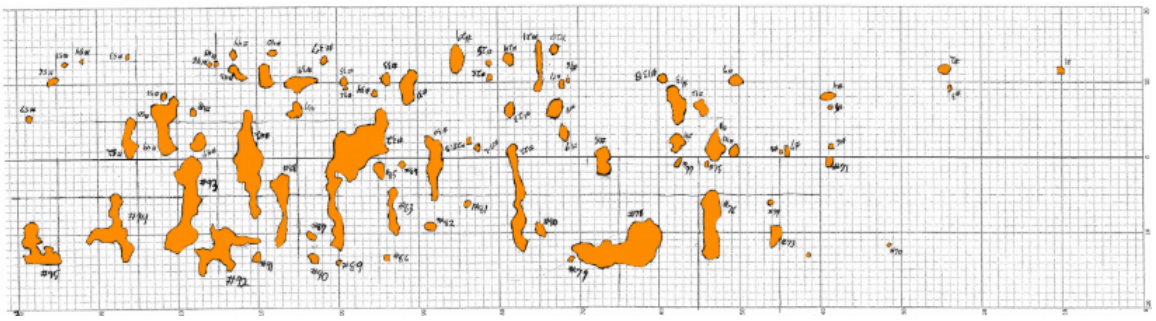

Fig. 1.2. Example map created from observing manually placed markings on a bridge deck. This map is painstakingly drawn by hand on a sheet of paper

of rotations a wheel makes while traveling. Examples of NDE research that uses wheel encoders for localization include the following references [7, 13, 14]. Wheel encoders are effective at low speeds, but can have issues with wheel slippage, wheel bouncing, and the wheel diameter being temperature dependent. They are also dependent on the inspector following a straight path. Distance perpendicular to the direction of travel must also be manually recorded.

There are many types of GPS systems to help localize an NDE platform. Ordinary GPS systems are often accurate within 1-2 m. When greater accuracy is needed a Real-Time-Kinematic (RTK) GPS can be used to obtain centimeter level accuracy. RTK GPS uses the signal carrier phase of two GPS systems to determine cm-level distances between the two GPS systems. Most commonly used GPS system is configured to be a stationary base station and the second GPS is configured to be a moving rover attached to the NDE platform. An RTK GPS is undesirable in locations with poor GPS signal strength or in situations where setting up or referencing a base station is inconvenient.

Some NDE imaging techniques, such as infrared thermography, GPR and high speed imaging, allow for another method of localization. These techniques use computer algorithms to match features between measurements and reconstruct a model of the test site as shown in **Figure 1.3** [15]. Video, LiDAR and IMU measurements can also be used to determine position and are now becoming more common because of the rapid development of autonomous driving applications.

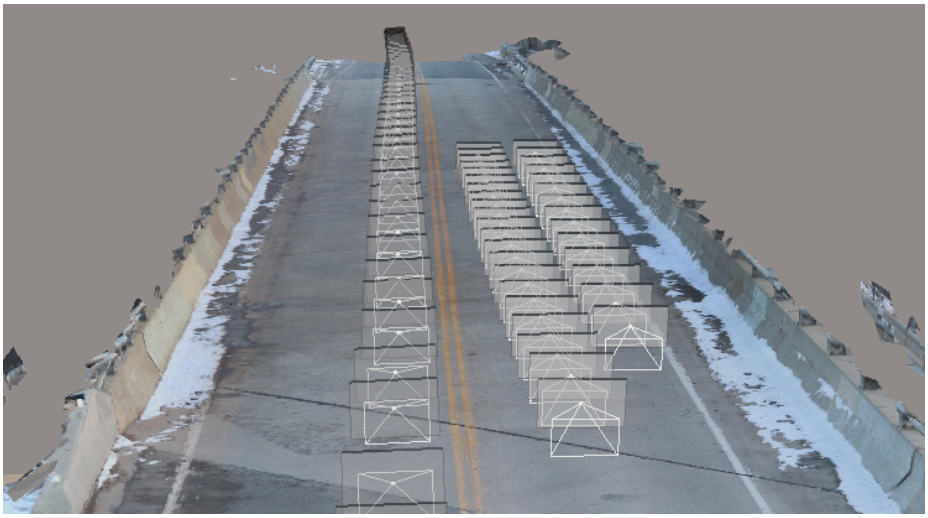

Fig. 1.3. A 3D model of a bridge reconstructed from multiple images. The location of camera for each images is represented as a gray rectangle connected to a pyramid.

1.2 Current and proposed NDE platform designs

Currently one of the most well known and developed NDE platforms is Rutger's Center for Advanced Infrastructure and Transportations (CAIT) RABIT platform [11, 16]. The RABIT incorporates GPR, high-definition imaging, ultrasonic surface wave, impact echo, and electrical resistivity sensors into an autonomous NDE platform. A GPS system attached to the RABIT allows for positioning of all the sensors. One limiting factor in the RABIT design is it that it is not readily adaptable to other NDE technologies, or improvements in the technologies already included on the platform. The speed of the RABIT is limited by the slowest measurement it performs. The RABIT must operate under permanent traffic control.

While the RABIT is a complete robotic solution, it would be desirable to have a modular NDE platform that can be operated at any speed and can easily connect or disconnect NDE technologies depending on the data to be acquired. Such platform should be able to localize on a bridge independent of the nondestructive testing data. It should also have generic input/output capabilities to allow for data collection from a wide variety of systems. The goal of this project was to develop such a platform.

This project provided a mobile platform design to allow Nebraska Department of Transportation (NDOT) to efficiently evaluate the condition of concrete bridge decks and improve maintenance and rehabilitation results. As shown in **Figure 1.4** , the proposed platform

was attachable to a standard receiver hitch and was to be comprised of several features, including three positioning technologies and a networking unit to accommodate various sensing modalities. This platform was constructed in Utah and deployed in Nebraska in Summer 2018. During the scanning tour, the platform was able to collect data and produce maps within minutes of acquiring the data. This work demonstrated the convenience, speed, and success of the approach and its potential utility for NDOT.

Additional features of this work are the collection of multiple NDE data sets using vertical electrical impedance (VEI), ground penetrating radar (GPR), automated acoustic sounding, and high-resolution photography. These NDE technologies provide complementary information about the bridge deck conditions, and data fusion algorithms are presented.

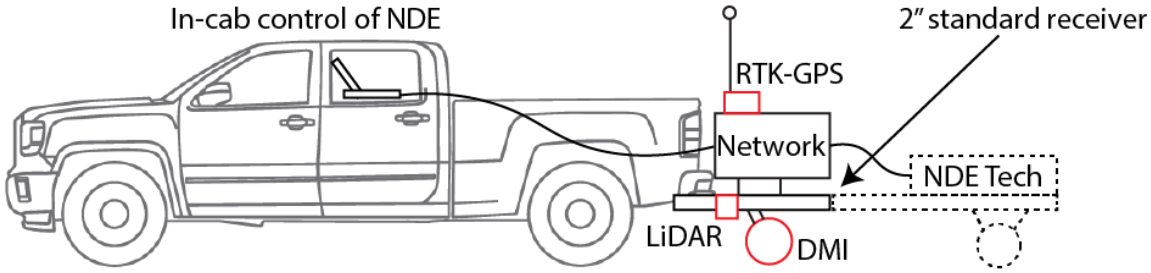

(a)

(b)

Fig. 1.4. (a) Originally proposed NDE platform to efficiently and easily collect NDE technology data during scanning. (b) Deployment of constructed NDE platform during scanning of a bridge on the Homestead Expressway in Nebraska during the 2018 scanning tour

1.3 Report overview

This report outlines the findings of the research conducted at the University of Nebraska-Lincoln (UNL) in collaboration with Brigham Young University (BYU) and Nebraska Department of Transportation (NDOT). **Chapter 1** summarizes the research objectives and background information of NDE platforms. **Chapter 2** presents the design of proposed multi-modal NDE platform consisting of localization and data collection units. **Chapter 3** introduces four NDT techniques, Vertical Electrical Impedance, Ground Penetrating Radar, Acoustic Scanning System, and High Resolution Imaging that were used in the research. **Chapter 4** presents the result of NDE platform and NDT techniques that are deployed on three bridges in Nebraska. All NDT methods, presented their findings in the form of condition maps for concrete bridge decks. In **Chapter 5** the results of NDTs are discussed, and compared. Also VEI, GPR, and acoustic maps are fused, and a condition map based on those methods is generated. In **Chapter 6** key findings from this project are presented and discussed.

Chapter 2

Development of NDE Moving Platform System

Localization of the measurement data was a considerable challenge throughout this project, and many of the project resources were devoted to developing solutions to this challenge. The difficulty lays in the desire to avoid placing any items, such as a base station, on or near a bridge deck so that a completely mobile solution was obtained. Because this excludes electromagnetic beacons and real-time kinematic (RTK) base stations (which also have trouble in canyons and other challenging multi-path terrains), a combination of technologies was needed to perform accurate localization.

The data collection framework for the Vertical Electrical Impedance scanner was custom-built to allow localization to be performed quickly after obtaining NDE data in the field. An overall schematic of this data collection framework is displayed in **Figure 2.1**. This system can also be used to control other open source NDE data collection systems.

2.1 Data collection unit

The data collection framework consisted of multiple single-board computers (SBC) that were linked together to acquire data from many different channels. A photograph of the rack that held all of these units is shown in **Figure 2.2**. The NDE units were individual channels configured specifically to log their data in this framework synchronized with positioning data acquired from a global positioning system (GPS), a light detection and ranging (LiDAR) system, and a high-definition camera. After an NDE scan was completed, the data could all be downloaded to a master controller computer by requesting the data

from the different SBCs through the network switch.

2.2 Localization unit

A key component of this data collection framework was a box containing the different measurement units that was placed between the NDE scanner and the towing vehicle. This localization box is shown in **Figure 2.3**. In the box is a microcontroller board that interfaces with two single-channel LiDAR units. These LiDAR units were positioned with quartz windows through which they could measure the distance to the parapet walls on either side of the bridge. Additionally, the box contained a high-definition camera pointed downward at the deck surface. In conjunction with this camera was a set of laser diode units that created a visible distance measurement on the deck surface. The camera and lasers formed an additional optical flow system that could compute the distance traveled.

In a post-processing algorithm, the differential global positioning system (DGPS) data were augmented with the LiDAR measurements and the entrance and exit timings provided by the camera to estimate the position of the NDE scanner on the bridge deck. More specifically, positioning relied on a continuous-discrete extended Kalman filter with a Rauch-Tung-Striebel smoother. The states of this system were the longitudinal location, transverse location, and heading of the moving platform. Additionally, the longitude and latitude of the bridge origin, the bridge width, and the orientation of the bridge were appended to the state space as biases and were also estimated. The states of this system were propagated in continuous time through a simple velocity-based motion model using Euler integration and a first-order interpolation for the sampled velocity obtained from the GPS information. Combining all these data streams in this framework allowed the system to accurately map NDE data to specific positions on the bridge deck.

2.3 Master controller software

The master controller software is meant to control slave controller software across a ethernet LAN connection. This software uses a GUI with several sections which perform different tasks are marked by colored rectangles in the **Figure 2.4**. The followings describe the tasks of each section:

- Red: Control of the naming conventions used in recording the data.
- Blue: Start and stop commands for recording as well as time stamping interruptions and importing measured data.

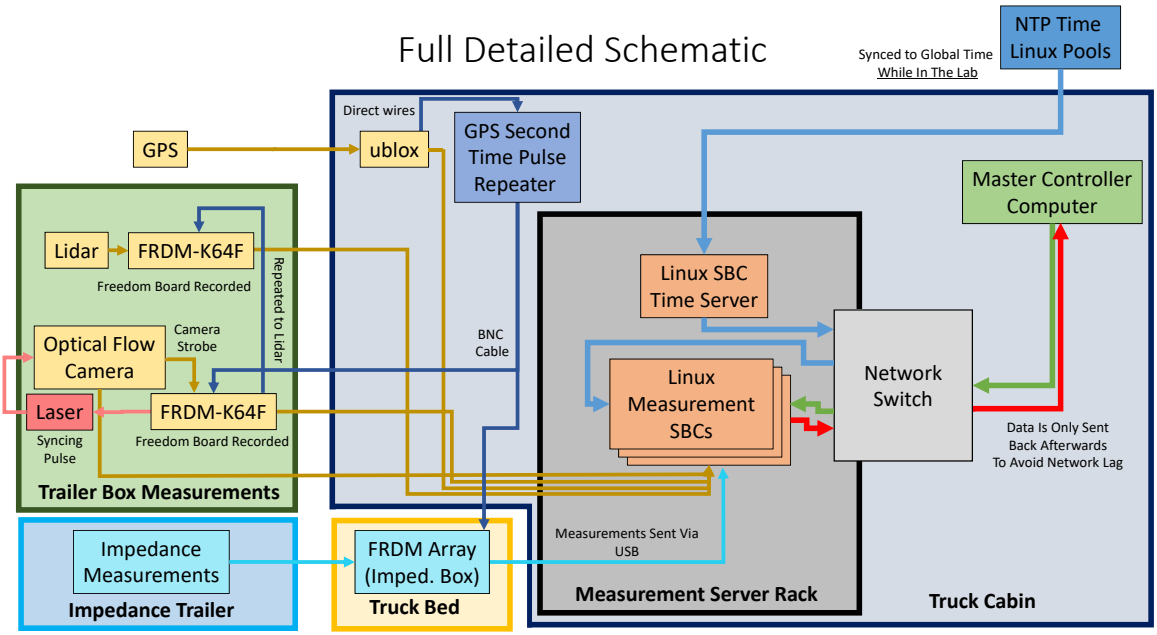

Fig. 2.1. Schematic of the data collection framework for the VEI scanner, with VEI, GPS, LiDAR, and camera measurements being recorded on different SBCs during scanning.

Fig. 2.2. Modular data collection system in which the SBCs are placed at the top of the rack, the network switch is in the middle of the rack, and power distribution and batteries are at the bottom of the rack

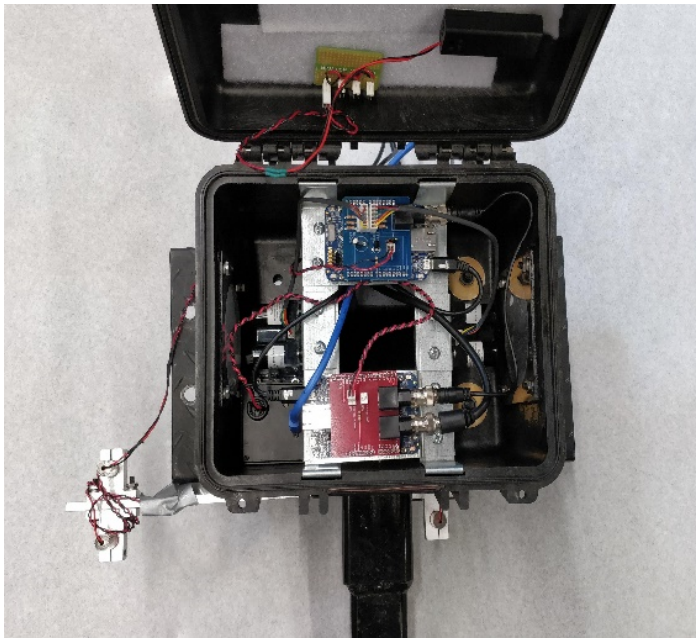

Fig. 2.3. Localization box containing a laser ruler, two LiDAR measurement units, and a high-definition camera used during scanning.

- Green: Contains the feedback section from the connected computers.
- Purple: Contains the connecting controls for connecting to a slave computer.

Naming Options

The first section of the controller has the naming section (shown in red). This section organizes the scans called "Passes" into a folder named after the bridge name and the current date. Multiple bridge names can be stored and switched between. These Names are stored in a text file "BridgeNames.txt" which can be deleted from the folder in order to remove all previous bridge names. The Pass number will attempt to increment upon selection of the "Stop Rec" button on the Recording section below. Like all of these boxes, any data can be placed inside and used to name the pass, however, the pass number will no longer increment automatically.

Combined with the pass number, a Lane designation is also added to the folder name. There are buttons to control this selector automatically. This includes flipping the direction North Bound(NB) to South Bound(SB) after each pass, (however box can be manually entered as well). There is also a minimalistic visual demo of the controller displayed within the window. The Star is representative of the current location within the lanes with the

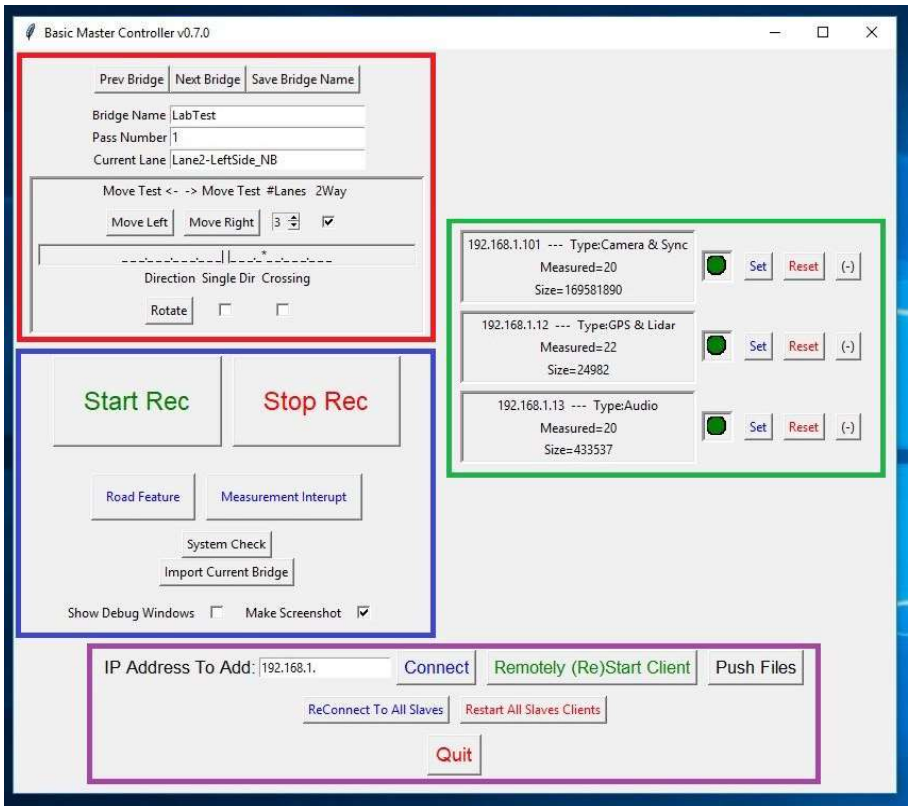

Fig. 2.4. Master controller software interface

periods representing Lane markers and the double line representing the yellow center. The following bullet points describes the keys and check points of the Naming section:

- Move Left/Right: Move the description of the current location left or right.
- #Lanes: The number of lanes in the current road
- 2 Way: The road in question is a connected road/highway with oncoming traffic.
- Direction: This Rotate button rotates the current direction (which is then updated after each pass unless the following option is selected).
- Single Dir = If this is selected, then the Direction will not update after each pass.
- Crossing: This option allows the description to allow the marker to cross into oncoming lanes.

Data Collection Controls

The data collection section which controls the overall **Start** and **Stop** commands for recording data is shown in blue color box. There are also blue timestamp buttons to record some sort of measurement interrupt or feature on the road that is wished to be noted. These are recorded only within the timestamp section of each slave computer. The **System Check** button performs a 3 second recording on all systems and will automatically import the data for inspection within the "Imported Data" folder created. The **Import Current Bridge** button will attempt to import all the data from all computers for the bridge currently at the Bridge Name section at the top for the current day.

The Debug Window option will result in the ssh protocol (plink.exe) being left open after remotely starting or restarting any slave computer. This is used primarily as a debug system.

The automatic screenshot that is created at the end of each recording can be disabled by deselecting this option which will allow the computers to finish their recording and begin responding again.

Computer Feedback Panels

The feedback panels which provide current feedback from the slave computers is shown in the green box. These panels will display the computer IP address as well as attempt to display what that computer is recording. However, if the computer is being slow to start up then this may show the error "Unknown even if it has started up correctly", regardless a reset of that slave client is advised.

Before starting recording the panels will appear with a Yellow indicator and "Not Init(ialized)" size of recording. The Measured speed section should display a number 10-12. While recording the panels will appear with a Green indicator and a slowly increasing size of recording (in bytes). The Measured speed section should display a number 20-22. If for any reason the slave controller completely crashes then the indicator will be greyed out and the Measured and Size sections will be blank.

Connection and Reset Options

The final section of the GUI is the connection settings which allow for connections to a IP address. The IP Address will be the computer that is controlled by the buttons shown in the purple box.

The **Connect** button attempts to connect to the already running slave code. However if the slave controller python code on the slave computer is not running this will not connect.

The **Remotely (Re)Start Client** will start or restart the slave controller python code on the slave controller. This allows for remote start-up without needing to VNC into the computer. However, this requires the remote computer to start up the python code which is much slower.

The **Push Files** button will push all files within the PushFiles folder in the running directory. This will overwrite any files in the home folder of the slave user. This is recommended for updates to the code.

The **Reconnect To All Slaves** will disconnect and reconnect to all the slave controller python codes. However the python code on the slave is not restarted. This is useful to reconnect to slaves if network connection is interrupted, but the slaves are still running.

The **Restart All Slaves Clients** button will close the slave controller python code on all the slave computers and restart them all afterwards. This is significantly slower and it is recommended if a slave crashes that that individual computer is restarted, not the entire set of slaves.

Chapter 3

Nondestructive Testing Techniques

In this research work four NDT technologies, Vertical Electrical Impedance (VEI), Ground Penetrating Radar (GPR), Automated Acoustic scanning system, and High Resolution Imaging for surface crack detection are introduced and described in details. GPR system and high resolution cameras are commercially available. The VEI system has been developed at Brigham Young University [12, 13], and the automated acoustic scanning system at the University of Nebraska-Lincoln [10, 17].

3.1 Vertical electrical impedance

Vertical Electrical Impedance (VEI) is an NDE technique to measure the protection offered to steel reinforcement against chloride ion ingress [12–14, 18–21]. A VEI measurement is shown schematically in **Figure 3.1**. An AC voltage potential is applied to the deck and electrical current from the center electrode of a guarded probe is measured. From the voltage and current applied to the deck, the impedance of the bridge deck to the reinforcing steel is estimated.

Impedance testing can provide quantitative information about concrete bridge deck condition. In the context of this work, impedance testing implies the measurement of the in-phase (resistive) and out-of-phase (reactance) current that is measured when an alternating potential is applied to a material. Because an alternating potential is used, the frequency at which interrogation is performed is important. For example, at very low frequencies (below 1 Hz) the interfacial impedance between an electrode and the concrete may be dominant, whereas at high frequencies (above 1 MHz), the capacitive properties of the concrete take on greater prominence. This frequency dependence can be an advantage

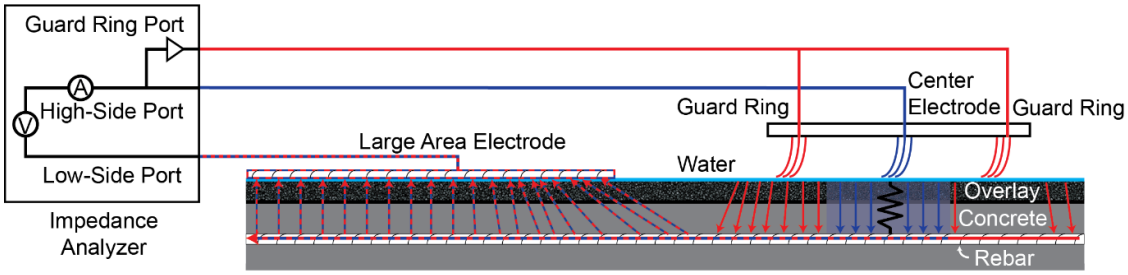

Fig. 3.1. A diagram of VEI in which the impedance of a constrained section of concrete directly beneath the probe is being measured.

for impedance testing because selection of the frequency can be tuned for the particular concrete condition or other conditions of interest.

Impedance is a suitable method to characterize concrete because the electrical resistivity of concrete is largely a function of the properties of the concrete matrix and the pore water. A concrete matrix with high porosity characterized by high interconnectivity and low tortuosity allows for the passage of high amounts of electrical current and would have low resistivity compared to a concrete with low porosity characterized by low interconnectivity and high tortuosity, all other factors constant. Regarding the pore water, high ion concentrations and high temperatures allow for the passage of high amounts of electrical current through the concrete due to the high abundance and mobility of current carriers. Impedance testing is an appropriate method for assessing concrete quality because the development of corrosion currents in concrete is also largely a function of the properties of the concrete matrix and the pore water. Higher porosity, moisture contents, chloride concentrations, and temperatures are all consistently correlated with higher corrosion rates and are manifest by lower resistivity values against chloride ion ingress. Resistivity values can consequently be useful for identifying areas of deteriorating protection of the reinforcing steel.

VEI is a useful NDE technique since electrical impedance measurements is inversely proportional to the diffusivity of ions through the bridge deck. Low impedance indicates locations where the deck is susceptible to chloride ingress, rebar corrosion, and formation of delaminations.

3.2 Ground penetrating RADAR

Ground Penetrating Radar (GPR) is a widely used NDT method for concrete bridge deck evaluation. A GPR antenna emits high frequency electromagnetic waves into the concrete

and receives the reflected waves from dielectric interfaces such as rebars. Advancements in the GPR instruments enable scanning concrete bridge decks in a relatively short time and store the data for further processing.

A GPR system generally consists of a control computer and an antenna. The computer provides power to the antenna, set measurement parameters, and stores recorded data. The antenna box contains a transmitter module to send electromagnetic pulse and a receiver to receive echoes from surface and subsurface interfaces. Meanwhile an external Real Time Kinematic (RTK) GPS system [22] attached to the GPR survey cart provides real-time positioning during the scanning.

A survey cart, shown in the **Figure 3.2**, is used in ground-coupled GPR survey. Since the survey is at a walking speed, traffic control is needed. The center frequency of the antenna determines the maximum penetration depth of EM wave and the vertical resolution of the B-scan image. Increasing the frequency will improve the image resolution at the cost of decreasing the penetration depth. In most bridge deck surveys, ground-coupled antennas with a center frequency of 1.5 GHz provides sufficient penetration depth and adequate resolution. The time range determines the total time that GPR records the reflections from the subsurface. The proper time range can be determined by the expected penetration depth and velocity information.

(a) GSSI SIR-4000 computer **(b)** GPR system on a survey cart

Fig. 3.2. GSSI-4000 GPR system.

Figure 3.3 shows a GPR B-scan images recorded over a bridge deck with 8 ns time range in the vertical scale. As highlighted in the **Figure 3.3**, direct coupling, rebar reflection, and bottom of the bridge deck are the main features that can be visually identified in the image.

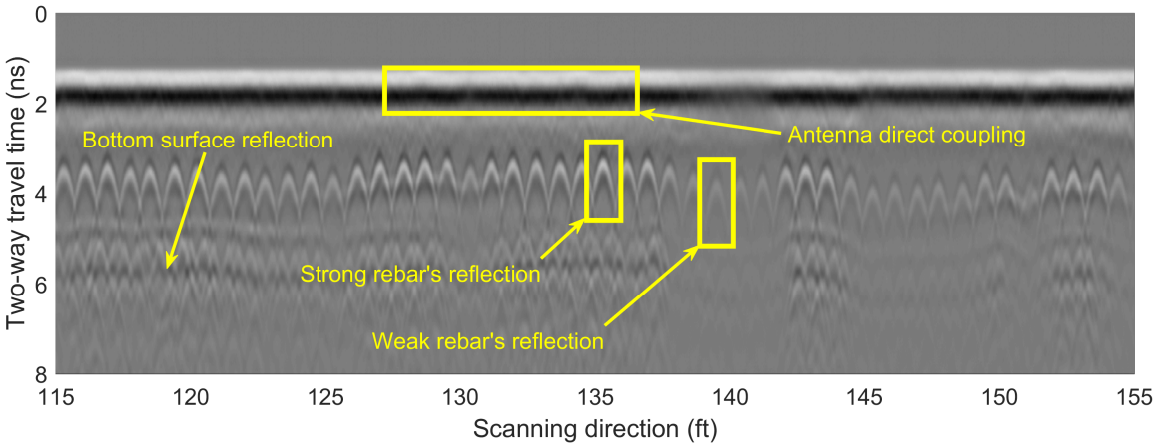

Fig. 3.3. GPR B-scan image

The conventional way to analyze the B-scan is through comparison of depth-corrected amplitudes of rebar reflections. Concrete deterioration and rebar corrosion will decrease the GPR amplitude and increase the attenuation. The UNL research team recently proposed a complete procedure for GPR data processing to address the issues in the current GPR analysis methods. These improvements include accurate zero offset, migration of rebar reflections, amplitude correction based on actual rebar depth, and accurate wave velocity, etc. Details can be found in recently published research reports and publications [23, 24]. With the new GPR analysis algorithm, we are able to extract three additional maps from GPR data, direct-coupling amplitude, wave velocity and cover thickness maps.

The direct coupling amplitude map represents the condition of the bridge deck surface. According to studies by [25, 26] the early GPR signal attributes (direct coupling wave) are sensitive to the permittivity and conductivity of the medium when a ground-coupled antenna is used. The observations in [24] indicate that direct coupling amplitude map is informative about the concrete surface condition which may be confirmed visually.

EM wave velocity in a dielectric medium is a function of electrical relative permittivity. Permittivity of water is several times greater than concrete material. Thus EM wave travels in wet concrete at a speed slower than it travels in dry concrete. Since, wet concrete provides a suitable environment for rebar corrosion, low EM wave velocity can be a precursor for concrete deterioration. In real concrete structures, wave velocity profile in concrete along the scanning direction is not constant, which depends on the concrete condition. Once the wave velocity is calculated around every individual rebar [24], and TWTT is obtained from the GPR system, cover concrete over the all rebar can be calculated. Then a cover thickness map is generated for the bridge deck.

3.3 Acoustic scanning

The acoustic scanning system includes an array of excitation sources and acoustic sensors (microphones), a data acquisition device, and a GPS positioning device. The work principle is based on measuring high amplitude acoustic response when a shallow delamination is subjected to impacts. In order to imporve the signal to noise ratio, a newly developed ball-chain was used as the excitation source [17]. The ball-chain is made of 12.7 mm and 15.9 mm diameter brass balls with a spacing of 25 mm. Smaller balls (12.7 mm) are used for delaminations with higher frequency and larger balls (15.9 mm) are for delaminations with lower frequency. In a previous study [17], the conventional steel link-chain and the ball-chain were tested on solid concrete surfaces and various delaminations. Comparison of these testing results shows that the ball-chain gave signals with higher signal-to-noise ratio (S/N) than the traditional steel link-chain. The difference is caused by different impact mechanisms from the ball-chain and link-chain. When a ball-chain is dragged on concrete surface, the balls jump and impact the surface randomly, and the impacts excite stress waves in concrete. The received acoustic signals are similar to the signals in the impact-echo test. In the conventional chain drag test, the link-chain mainly slides on the concrete surface, where the surface friction is the driving force for acoustic signals.

Fig. 3.4. 12-channel acoustic scanning cart

Low-cost MEMs (Micro-electro-mechanical systems) microphones (Adafruit SPW2430) with a nominal frequency range of 100 Hz to 10 kHz (actual frequency range is broader) were used as the acoustic sensors. The microphones and the ball-chains were installed on a 6-ft (1.8 m) wide scanning frame (see **Figure 3.4**). The testing frame includes 12 sensing channels with a spacing of 6 inch (0.15 m), and each channel includes one MEMs microphone and one ball-chain. The acoustic signals received by the microphone array were digitalized by two oscilloscopes (PICO4824 and PICO5444) with a sampling rate of 100 kHz and transferred to computer. Meanwhile a Real Time Kinematic (RTK) GPS system (Piksi GPS, Swift Navigation, Inc.) provided real-time positioning during the scanning. A LabVIEW program was designed to control the data acquisition of acoustic signals, and positioning data.

The scanning cart can scan a bridge deck in a normal walking speed (about 4 ft/s). With the scanning frame width of 6-ft, the system can scan an area of 24 ft^2/s. The longitudinal spatial resolution depends on the scanning speed. At a walking speed, this system will give a spatial resolution of 1-2 inch. The testing speed effect is discussed in detail in a previous study by the authors [17].

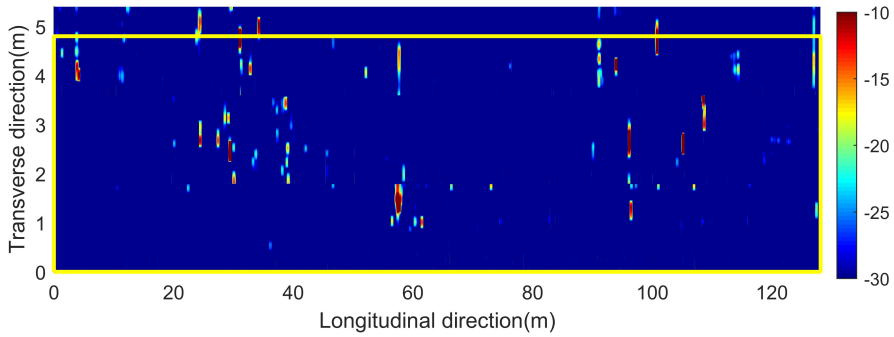

Fig. 3.5. Acoustic scanning results of a one lane bridge [10]

The acoustic signals from all channels were processed in frequency domain using short time Fourier Transform. The time axis was related to the GPS data to give longitudinal position of each scan, while the acoustic energy within the frequency range of 0.5-5 kHz is used to identify the delamination responses. The detailed signal processing algorithm are described in reference [10, 27]. Multiple channel signals from each scan can generate one 6-ft wide image, and multiple scans were then combined together to generate a full 2-D delamination map of the bridge deck. **Figure 3.5** shows an example of the acoustic

scanning result of a one-lane bridge. In the figure, blue area represents sound regions of a bridge deck and red spot are delaminations.

3.4 High definition images

A typical image data processing pipeline for detecting deficiencies (such as crack) based on non-contact optical sensors consists of three major tasks: 1) data acquisition, 2) localization, and 3) crack detection. The possible types of input data for data acquisition are image sequences, GPS, odometer, and LiDAR data. First of all, the data acquisition speed for such systems is dependent on the speed of optical sensors and the moving platform. The ideal system should be able to acquire data in a fast and simple way without obstructing traffic. Secondly, the localization task may typically rely on the GPS or odometer sensor data. However, odometer sensor data can provide relative position along the direction of traffic but not the position in the transverse direction, perpendicular to the direction of traffic, and it is well known that the GPS is not always available or GPS does not provide the pose information. For such reasons, this study focused on providing an alternative localization strategy through high definition images. Lastly, for the detection task, various approaches have been proposed in previous studies including a simple image processing or machine learning based approach [28–31]. Regarding detecting cracks, which is the focus of this study (to find transverse cracks), most of the existing detection methods are based on a low-intensity and localized line-segment characteristics of cracks. This method will not be efficient in successfully categorizing "cracks" and "non-cracks". To improve existing approaches, other characteristics such as the direction or shape of the cracks should be considered in a smarter machine learning approach. There have been many recent studies focusing on crack detection techniques through image processing and a detailed literature review is provided in one study [32].

However, most of these studies focused on improving crack detection and not necessarily applying their methods for the entire deck and only providing information for a local area. It would be much useful to be able to identify where the specific crack is located within the bridge, what the average and maximum crack widths are, how long the cracks are, and what the shape (direction) of the crack is to assess the damage level and causes of them. For example, by observing the shape and directionality, it will be possible to identify whether it is a material or a structural crack. By having the length information, one will be able to identify whether the crack is a primary crack or a secondary crack. Crack widths and spacings would also be useful information that inspectors would like to know. Most of the

existing crack detection systems are not providing many of these essential data which is one of the reasons bridge owners are not fully utilizing these techniques. In this research, we have developed a computer vision-based crack mapping system that can provide all of the essential and critical information listed above (crack location, number of cracks, crack spacings, crack widths, crack length, and shape of the crack) by collecting high definition images. The system collects thousands of high definition images from a bridge deck with machine vision cameras attached to a road vehicle. And it produces not only a global crack map which provides the location of the cracks, but also the local information for each crack including the orientation, width, and length.

To achieve the resolution of the widths of typical cracks (average crack widths measured in bridge decks are approximately 20 mils; 0.020 in.) observed in bridge decks and to be able to provide the location of each crack, we have employed a multi-view, multi-resolution camera system. The system uses 3D computer vision-based localization and mapping technique. Two cameras have a wide field of view (angle) for localizing frames in both longitudinal and transverse directions. The other two cameras have deeper focal length and can capture high resolution (detailed) images of the cracks. **Figure 3.6** shows the overall process of the proposed approach. The processing pipeline looks similar to those of other conventional approaches. But our system collects multi-view image sequences as input. And the techniques used in the subsequent steps are different and designed to achieve fast deployment and high accuracy in measurements and mapping cracks.

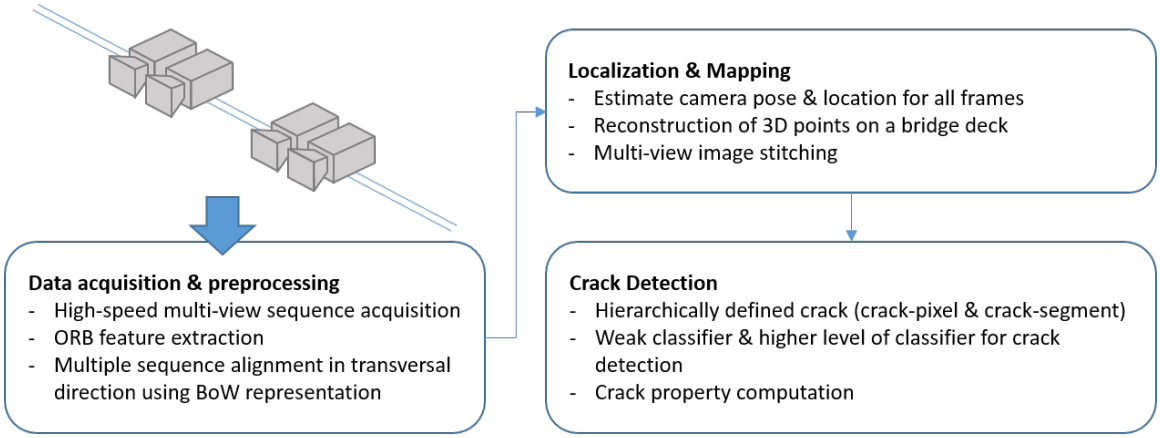

Fig. 3.6. Overall process of the proposed system

One of the challenges in making detailed measurements and localization during high-speed acquisition is that the relative pose (in 3D) between the four cameras and the surface of a bridge deck continuously changes. Therefore, the localization is completed by recovering

the camera pose and location in 3D for every single frame and reconstructing the 3D surface of the bridge deck, without using GPS data.

For crack detection, unlike other approaches which is based on a relatively simple definition or assumption for cracks in images (e.g. line segments with low intensity pixels), we used multiple hierarchical characteristics to define cracks. At the lower level, we defined a crack-pixel that has low-intensity value and has a dominant orientation. At the higher level, we defined a crack-segment which is a sequence of crack-pixels, or a sequence of crack-segments, recursively. According to the hierarchy, we have applied two levels of classifiers. The crack-pixels are over-detected by a weak classifier. Once they form crack segments, the higher-level classifier determines the labels based on the features obtained from each crack-segment.

Chapter 4

Field Demonstration

Field demonstrations of the NDE techniques described in **Chapter 3** were performed in August 2018 to evaluate bridge deck conditions on three bridges in Nebraska. These three bridges have concrete bridge decks with different overlays, including bare concrete, concrete overlay, and asphalt overlay, which represent the typical deck types in Nebraska. Each bridge was tested for about 3 hours with traffic control. The VEI system was connected to the NDE platform data collection unit and positions of the VEI measurement were recorded by localization unit.

After NDE tests on the bridges, chloride testing was also performed to measure the chloride content of the concrete at designated locations. Chloride concentration testing is a destructive evaluation technique that involves measuring the chloride concentration in the concrete of a bridge deck. During chloride concentration testing, a small portion of the concrete is pulverized (usually with a rotary hammer) and the powder is collected for laboratory tests in which the concentration of different molecules can be ascertained. Chloride concentration testing should be performed at multiple depth intervals. When chloride concentration exceeds a specific 2 lb/ft^3 at the depth of rebar, the rebar starts corroding.

The following sections present description of bridges with the NDE and chloride concentration test results with their locations.

4.1 Test procedures

The vehicle mounted imaging system can scan the bridge deck at a normal traffic speed. Thus, the bridge deck surface images were first collected by the high definition imaging

system. Since the VEI system require soaking the bridge surface with water, and GPR and acoustic scanning might be affected by standing water on surface, the VEI test was the last test on each bridge. The GPR and acoustic scanning tests were performed at a walking speed. GPR requires multiple scans over the bridge with 1-2 ft line spacing. The acoustic scanning system had a 6-ft lateral span, which needs 2-3 scans to cover one driving lane plus the shoulder on each bridge. The locations of both GPR and acoustic test were recorded by the RTK GPS.

4.1.1 Vertical electrical impedance test

VEI measurements were obtained using the VEI apparatus shown in **Figure 4.1**. The VEI apparatus included six impedance probes that collectively spanned 12 feet. Each probe collected 100 impedance samples a second as the platform crossed the bridge at 2-3 mph. The VEI apparatus's watering system wet the bridge with approximately 15 gallon of water per minute to allow better electrical coupling between the probes and the concrete. The NDE platform collected data that was used for localizing each impedance measurement to a spatial location on the bridge deck.

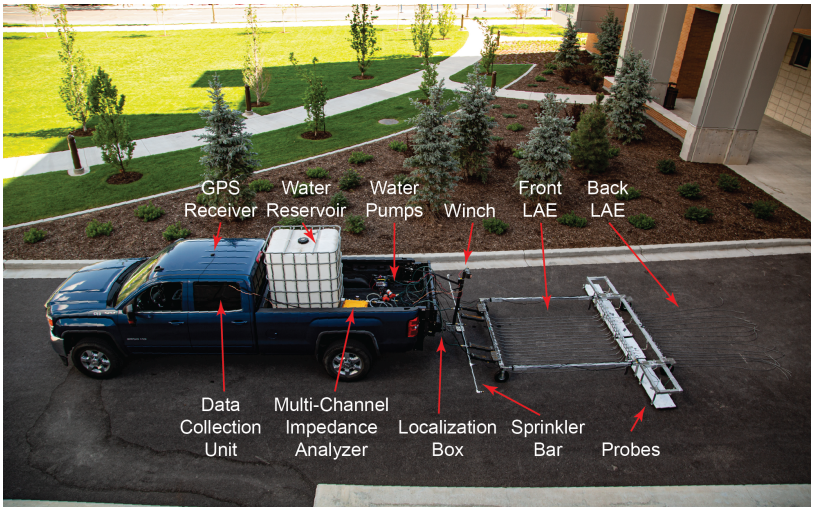

Fig. 4.1. Photograph of the VEI apparatus.

Immediately after impedance scanning was performed, preliminary impedance maps were generated to enable identification of a low-impedance location and a high-impedance location on each deck for chloride concentration testing. At each location, two chloride concentration samples were obtained using a rotary hammer. The first sample represented

the depth interval from 0 to 1 in., while the second sample represented the depth interval from 1 to 2 in. After removal, the samples were returned to Brigham Young University for laboratory analysis. Photographs of the hole and patched hole for the low impedance location of Bridge Deck 1 (S006 29351) are found in **Figure 4.2**.

(a) **(b)**

Fig. 4.2. Photographs of a hole made for chloride sampling (a) and the patched hole (b) after sampling was complete.

4.1.2 High definition imaging

We used multiple optical sensors attached to a road vehicle for data acquisition as shown in **Figure 4.3**. Two types of optical sensors (cameras) were used where one serves for localization and the other for crack detection purpose. For image-based localization, two large field-of-view cameras were used to cover a wide surface (bridge deck) area and to compensate the relative pose changes through performing stereo reconstruction of 3D points on the bridge deck in real-scale. The other two cameras were used for crack detection and have a longer focal length to capture the surface of bridge deck with high resolution images (provides two-times finer resolution than the other pair of cameras).

The typical width of a pixel projected on the ground, w_c, should be smaller than the (desired) minimum measurable width of cracks as shown in **Figure 4.4 (a)** to increase the accuracy of crack measurements, where w_s is width of the sensor, n_p is the number of pixels, f is the focal length, and d is the distance between the focal point and the target surface. Another important factor that affects the accuracy of the measurement is motion blur caused when the vehicle is moving at high speed. In **Figure 4.4 (b)**, Δt represents the exposure time and v is the speed of the vehicle. During Δt, the proportion $(b_0 + b_2)/(\Delta t \cdot w_c)$ of the

Fig. 4.3. Multi-view Camera System mounted on a Road Vehicle

value of one pixel is obtained and accumulated from the adjacent area and this creates blur around the boundary of a crack pixel. The smaller Δt is the blur will decrease. However, noise will increase under low illumination conditions. In that case, additional light source is required to decrease the noise level.

The four imaging sensors capture multi-view sequences along the direction of traffic. The sensors are synchronized by a trigger signal. The i^{th} sequence s_i consists of multi-view frames f_i, j, $(0 \leq j < n_i)$. Each frame has four images I_0, I_1, I_0^h, and I_1^h. The images are undistorted using the distortion parameters. The frames have an order in their sequences but they do not have information about adjacency to other sequences in transverse direction of the bridge.

We extracted image features for each frame of all sequences before the localization step. The main purpose of extracting features is to find pixel-level correspondences between frames and image-level correspondences among sequences. We have selected ORB (Oriented FAST [33] and rotated BRIEF [34]) which detects FAST corners and produces a binary descriptor of 256 bits for each feature point [35]. It is fast and simple but invariant to orientation changes. The features and descriptors are extracted after warping each image using a homography matrix which represents a mapping from the image to the ground plane and is obtained by sparse stereo matching [36]. This process decreases the scale differences within a frame or among frames generated by perspective projection or by the motion of the vehicle.

We performed two levels of image-based localization after collecting high definition images. First, we aligned the sequences in transverse direction and defined an adjacency

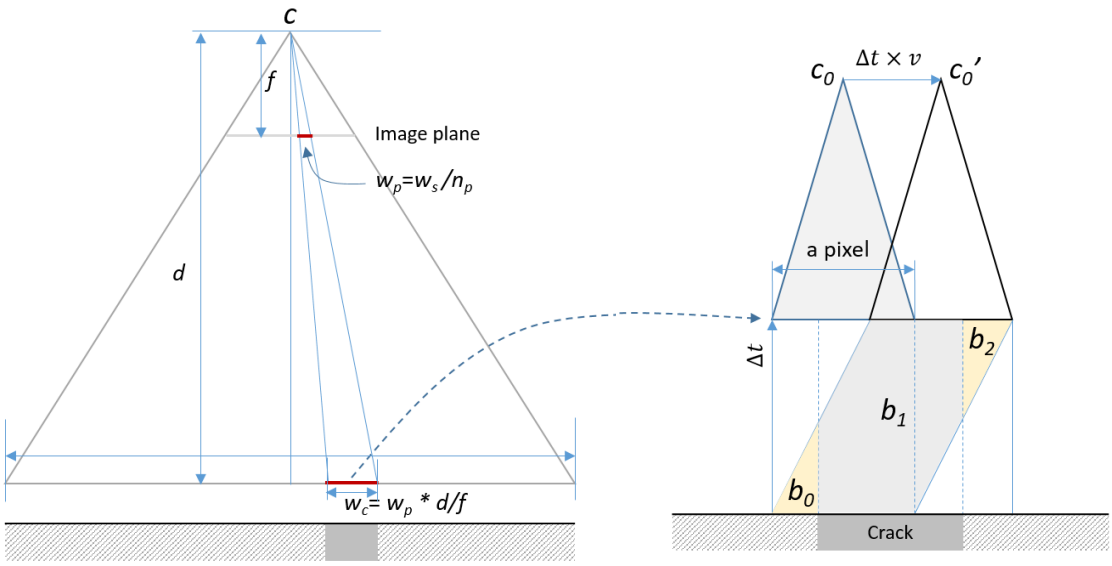

(a) parameters of imaging sensor

(b) vehicle motion and motion blur

Fig. 4.4. Parameters that control the accuracy of crack measurement

graph, $G = (V, E)$, including frames of all sequences. The vertex, V, is a set of all frames and a set of all edges, E consists of edges within a longitudinal sequence, E_L, and edges across transverse sequences, E_T

$$E = E_L \cup E_T, E_L = \{f_{(i,j)} f_{(k,l)} || i - k| = 1, j = 1\}. \tag{4.1}$$

E_T can be obtained by comparing features of a frame to those of all frames of other sequences. **Figure 4.5** shows the sequences and adjacency graph G with longitudinal and transverse edges E_L and E_T.

The second step for image-based localization and mapping was conducted to obtain 3D translation and rotation of each frame by traversing each node of the adjacency graph, G in breath-first order. As illustrated in 4.6, we reconstructed 3D points using 2D correspondences among views within a frame since our multi-view camera sensors are calibrated. Once, a frame has 3D information for enough number of 2D feature points, we can compute rotation and translation of an adjacent frame by searching for the 2D feature correspondences and solving a perspective-n-point problem.

In order to detect cracks from images, we have defined a crack hierarchy using crack-pixels and crack-segments as shown in **Figure 4.7**. The crack-pixel is the basic unit of the crack within an image. A crack-pixel has low intensity value and has a dominant orientation.

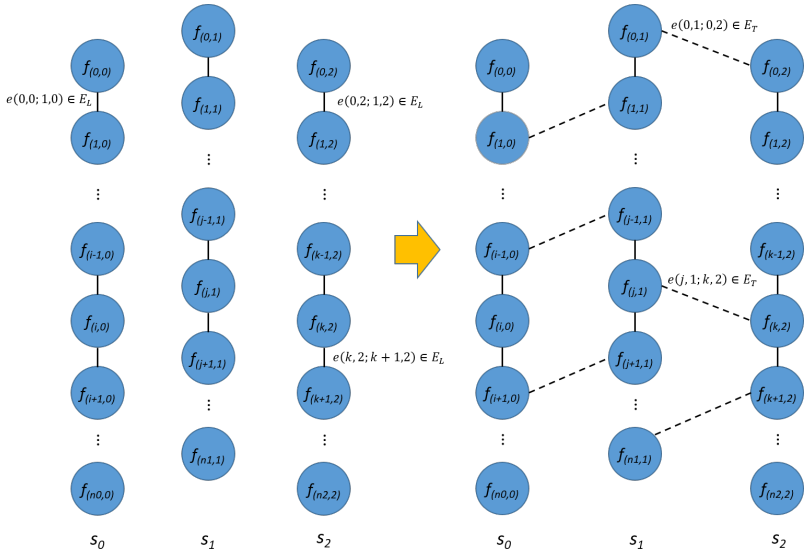

Fig. 4.5. Image sequences and an adjacency graph with sets of edges E_L and E_T.

A crack-segment is an ordered set of crack-pixels or it is recursively defined by a set of crack-segments. Each crack-pixel of a crack-segment should have the similar orientation with those of the neighboring crack-pixels. The relative position to the neighboring crack-pixels should be consistent with the orientations of them as well.

$$c(u,v) = (p(u,v), s, I(p), g(p), \theta, w) \tag{4.2}$$

where, $p(u,v)$ is the position of the crack-pixel in the coordinates of the stitched image, u and v indicate the position in transverse and longitudinal direction, respectively. s is the scale of the crack-pixel. $I(p)$ is the intensity value of the pixel, θ is the orientation, $g(p)$ is the gradient of pixel values in the perpendicular direction of θ, and w is the width of the crack.

Many of the previous research studies assumed that a crack has low intensity and the local shape can be approximated by a line segment. Our definition of a crack element is stricter considering the dominating characteristics of the pixels (low-intensity and a dominant local orientation) but more flexible (less strict) for the shape of the crack. By the definition of a crack-pixel and a crack-segment, each crack is represented by a tree structure as shown in **Figure 4.7**. The nodes of the tree are crack-segments and the leaf nodes have crack-pixels as shown in **Figure 4.7**.

The detection of cracks is completed in two steps. In the first step, we detected crack-pixels by examining the local image patch centered at each pixel. We prepared a scale-space

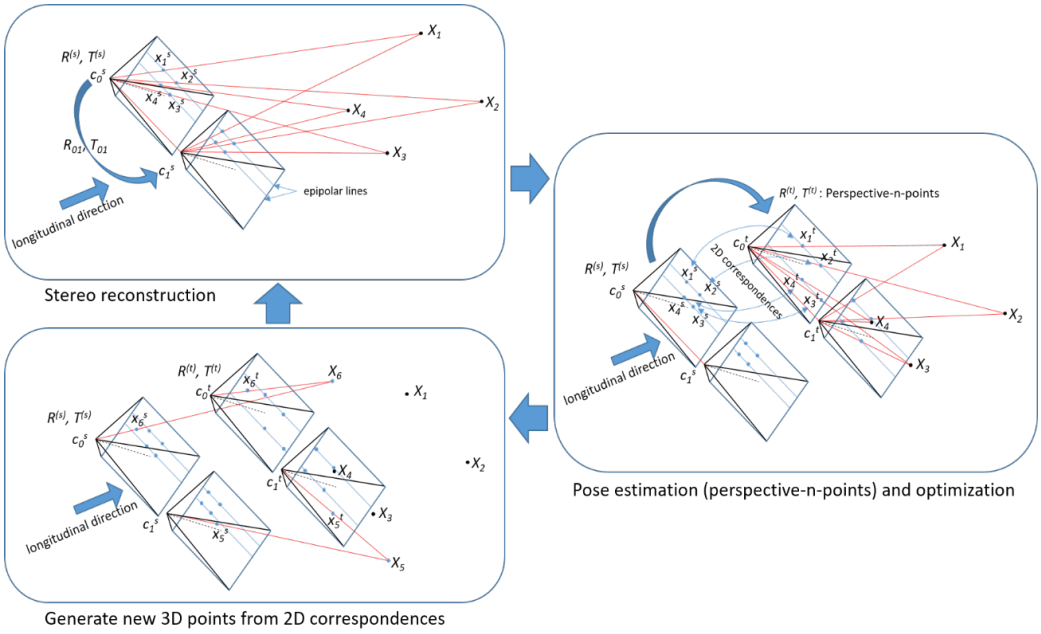

Fig. 4.6. Image-based localization and mapping.

to take into account different scales of cracks to detect the cracks greater than a single pixel. Then, for each pixel p_0, we built a circular histogram from the image patches of all scales to check whether the pixel has a dominant orientation of low-intensity pixels or not. Each bin of the histogram represents relative orientation of pixels within the patch. Each histogram accumulates pixel values along the relative direction of the pixels in the patch as illustrated in **Figure 4.8**. In the figure, $I(p_1, \pi/4)$ represents a pixel value of the pixel that is located at the direction of $\pi/4$ and has distance of 1 from the pixel p_0. We determined a dominant orientation by detecting two bins that have local minimums and averaging the corresponding orientations as shown in **Figure 4.8**. Once the orientation was determined, the gradient of pixel values to the perpendicular direction of the orientation was computed. In the figure, the average of $|I(p_0) - I(p_{1,0})|$ and $|I(p_0) - I(p_{1,\pi})|$ is the value of $g(p_0)$. The scale selection was done by comparing $g(p_0)$ values of the crack-pixels of all scales. The crack-pixel that had the maximum $g(p_0)$ and the corresponding scale was selected as the value of s for the location p_0. This weak classifier inherently produced false-positives because the properties we used for crack-pixel detection were not sufficient for describing a crack element.

In the second step, we formed crack-segments and classified them into cracks and non-cracks. For each detected crack-pixel, we counted the number of supporting crack-pixels that satisfies the following conditions: (1) the supporting crack-pixels should be within a

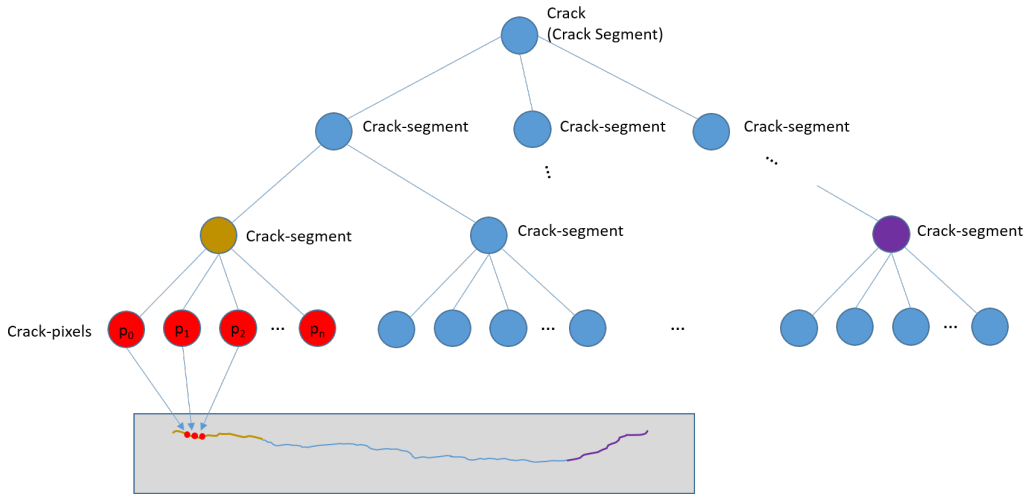

Fig. 4.7. Hierarchy of crack pixels and crack-segments

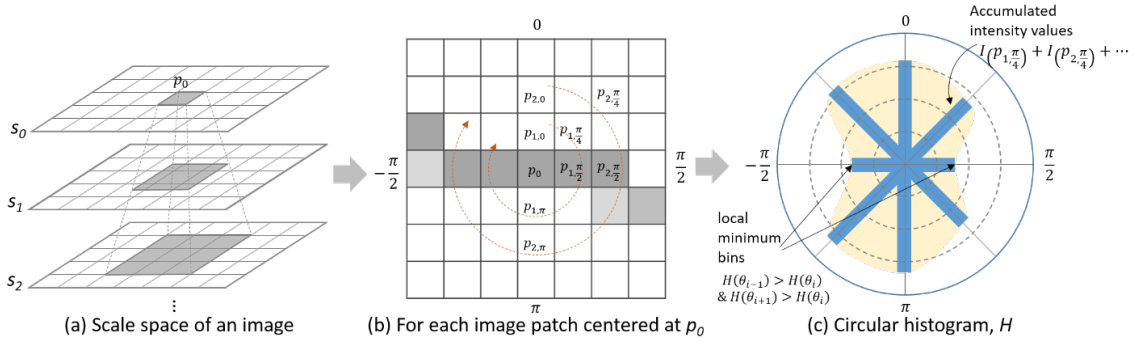

Fig. 4.8. Detection of a crack-pixel using an orientation histogram.

local window defined by a radius r, (2) they should have the similar orientation with that of the crack-pixel, (3) the relative direction of the crack-pixels with respect to the crack-pixel should be consistent with the orientations of themselves and the crack-pixel. These three conditions are represented in the following equations.

$$\begin{aligned} d = |p(x,y) - p(x_i,y_i)| < r, \\ |v_i \cdot v_o| > \cos\theta_s, \\ \min\left(|\theta - \theta_i|, \frac{\pi}{2} - |\theta - \theta_i|\right) < \theta_s \end{aligned} \tag{4.3}$$

where $v_i = (p(x_i,y_i) - p(x,y))/d$, $v_0 = (\cos\theta, \sin\theta)$, θ is the orientation of the crack-pixel p(x,y) and θ_i is the orientation of the i-th crack-pixel $p(x_i,y_i)$. θ_s represents the maximum

angle difference.

We initialized a crack-segment using a crack-pixel that has the maximum number of supporting pixels within a local window. This process is illustrated in **Figure 4.9**. For a crack-pixel c_0, the pixels c_i and c_j (blue-colored pixels) are the supporting pixels. But c_k is not a supporting pixel of c_0 because the vector v_0, k and the orientation of c_0 are different. Crack-segments will have a sorted list of crack-pixels, location, average orientation, length, and an average width. A sorted list of crack-pixels is obtained by projecting the pixels onto the principle axis of the crack-pixels (the direction that the crack-pixels are aligned with). We expanded the initial segments in two directions by adding crack-pixels that were not assigned to any crack-segments. Two end-points are the first and last elements of the sorted list of crack-pixels. In **Figure 4.9**, c_p is one of the end-points of an initial crack-segment s_0, and c_1 is a candidate crack-pixel which can be included into s_0. The crack-pixels that are not assigned to any crack-segments will be discarded. In the next step, crack-segments are compared and linked if end-points of two crack-segments are close enough and the average orientations of two crack-segments are similar (when it is less than θ_s). Existing approaches connects locally detected cracks which are mostly consisted of line segments, but the crack-segment defined in our study is an ordered set of crack-pixels detected through the clustering and linking process.

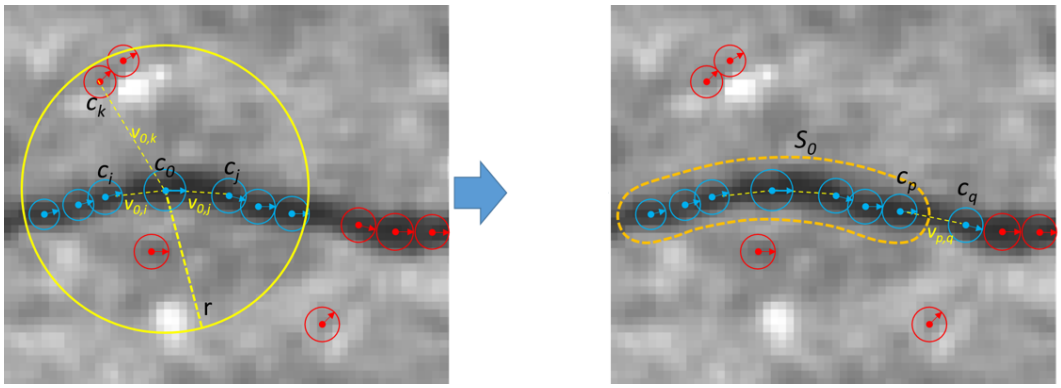

(a) **(b)**

Fig. 4.9. Crack-segment initialization (a) and expansion (b).

4.2 Bridge deck 1 - ID: S006 29351

Bridge S006 29351 was tested in the morning of August 1, 2018 in Milford, Nebraska. The satellite image of the bridge is shown in the **Figure 4.10**. The bare concrete bridge deck is 293 ft. long with two lanes and carry two way traffic. Due to time constraints at the time of testing, only the north bound lane and the shoulder were tested. Traffic control was provided on the northbound lane while southbound the traffic was open to vehicles. On this bridge deck four nondestructive testing techniques were deployed. Vertical Electrical Impedance, Ground Penetrating Radar, Acoustic scanning, and high definition imaging. The test results are presented in the following subsections.

Fig. 4.10. Google map picture of the bridge S006 29351 (map data ©2018 Google)

Vertical impedance scanning

The results of the two passes of VEI scanning on Bridge Deck 1 are shown in **Figure 4.11**. To evaluate Bridge Deck 1 with the VEI scanner, both the southbound lane and shoulder were scanned twice. During these four passes, 12.5, 12.3, 18.9, and 15.6 gallons of water were applied to the deck surface. These amounts corresponded to approximately 0.003 to 0.005 gallons per square foot. A prominent feature of the impedance maps is a long line of low impedance running the length of the bridge approximately 12 ft from the parapet wall. Visual inspection indicated that this line corresponds to a construction joint running the length of the bridge. Interestingly, this feature correlated with a similar feature in the GPR map. Other distinctive features prominently shown on the maps are multiple transverse lines, spaced every few feet along almost the entire length of the bridge. These features correlated well with observed transverse shrinkage cracks that occurred at fairly consistent intervals along the length of the deck. These transverse cracks were also observed in the GPR results.

From the data shown in **Figure 4.11**, soaking during subsequent scanning passes did not appear to significantly change the results between passes. For this bridge deck, the low-impedance chloride concentration sampling location was positioned at a longitudinal distance of 212 ft and a transverse distance of 15 ft, while the high-impedance chloride concentration sampling location was positioned at a longitudinal distance of 162 ft and a transverse distance of 9 ft. The results of the chloride concentration testing are shown in **Table 4.1** at the end of this chapter.

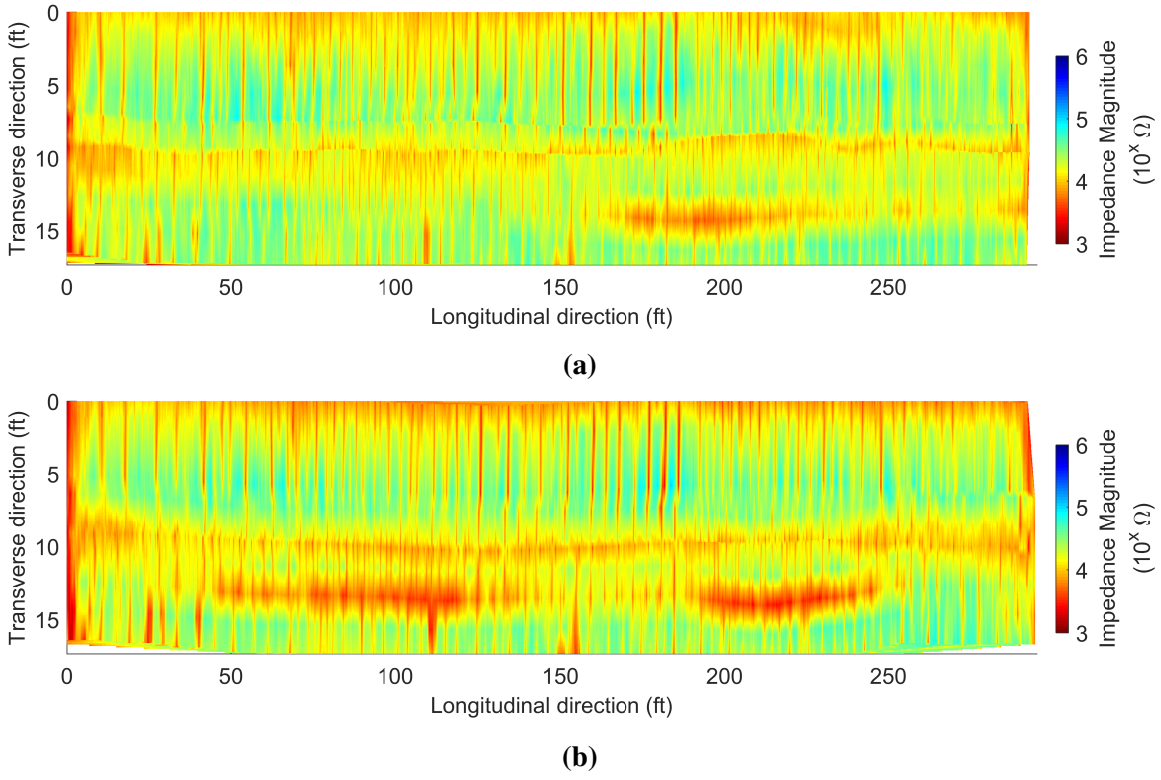

Fig. 4.11. VEI map of Bridge Deck S006 29351 generated from the first pass (a) and second pass (b) (Not to scale).

Acoustic

The acoustic system collected the data with 6 ft. coverage with and overall 3 scans collected to cover the north bound on this bridge. **Figure 4.12** shows the delamination map of the bridge deck. Acoustic images shows a few isolated transverse cracks (red color). The regions with light blue color indicate high level of traffic noise during the acoustic scanning.

No major delaminations are detected in this bridge deck.

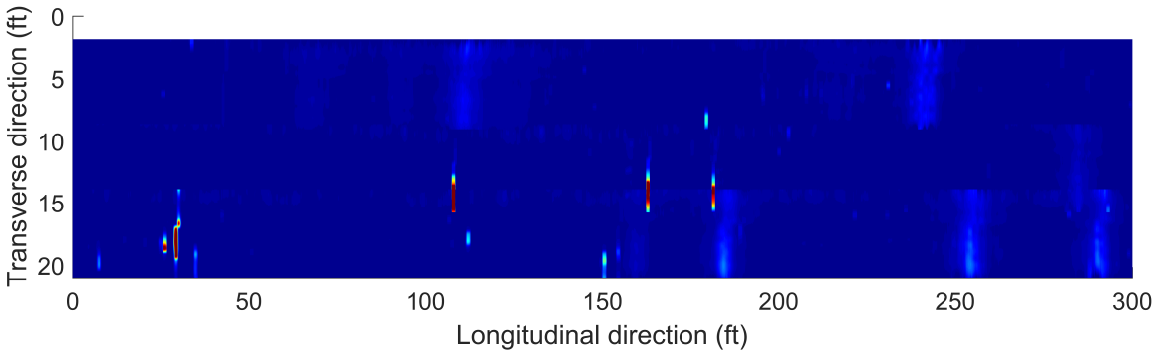

Fig. 4.12. Delamination map of Bridge Deck S00629351. (Not to scale).

GPR

A GSSI SIR-4000 GPR systems with 1.5 GHz antenna was used to test the northbound lane. The spacing between scan paths were 2 ft and 9 scans were recorded. The scanning positions were determined using RTK GPS [22] device mounted on the survey cart. From GPR data collected on this bridge, direct coupling amplitude, velocity, depth-corrected amplitude, and cover thickness map are generated as shown in the **Figure 4.13**. **Figure 4.13a** shows the depth-corrected amplitude map of the bridge deck. High attenuation of GPR amplitudes is highlighted by red color in the map. Red spots and transverse strips are widely distributed over the bridge deck, more high concentration between 125 ft. to 250 ft. in longitudinal direction. These red strips correspond to shrinkage cracks in the transverse direction. Very high attenuation is also seen along the joints. These patterns are consistent with the VEI results. **Figure 4.13b** shows the velocity map of the bridge deck. High moisture content of the concrete causes increase in permittivity of the concrete and lower EM wave velocity. Except a few localized spots on the bridge, the wave velocity is is within normal region. **Figure 4.13c** shows the direct coupling amplitude map of the bridge. Low amplitudes in this map indicates surface anomalies, and deterioration on the surface of the bridge deck. **Figure 4.13d** shows the cover thickness variation over the top reinforcement mat.

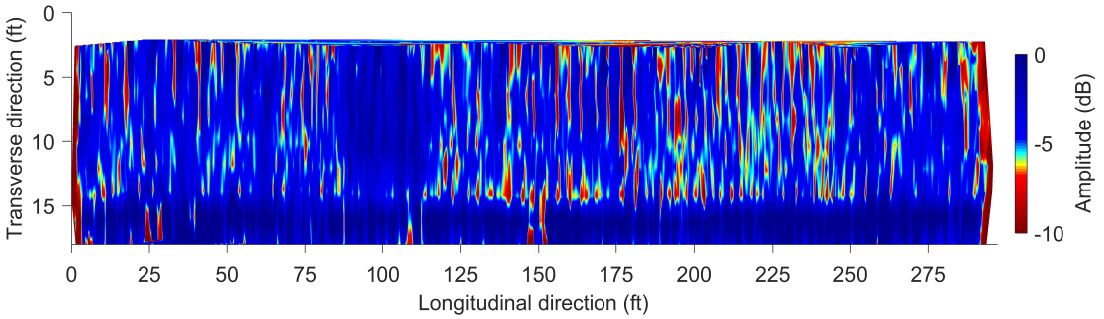

(a)

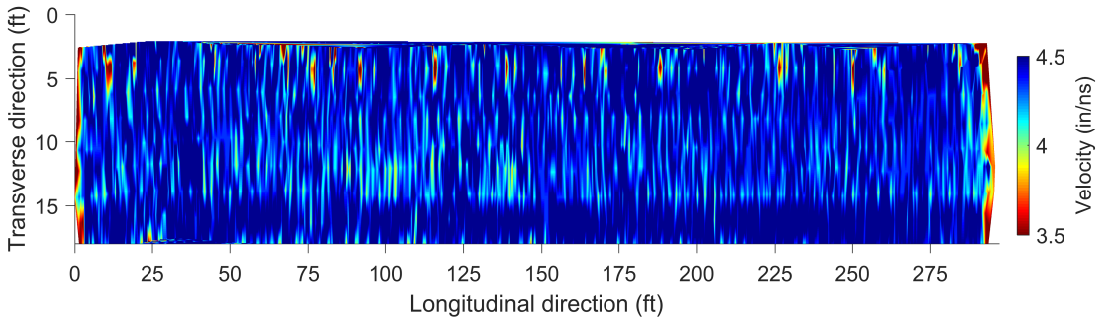

(b)

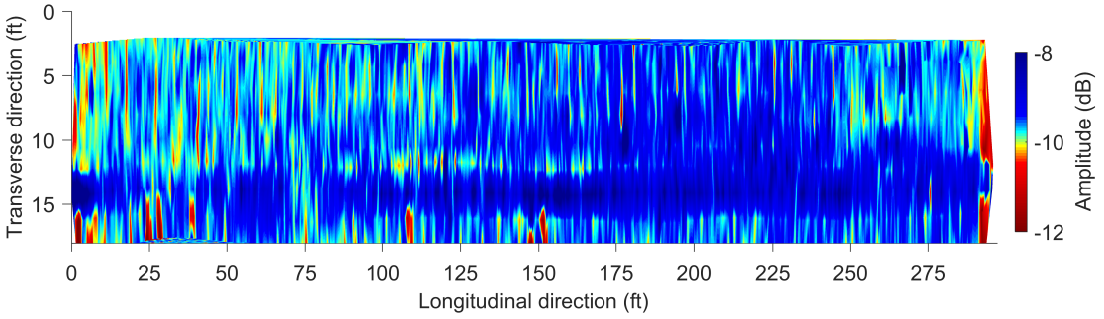

(c)

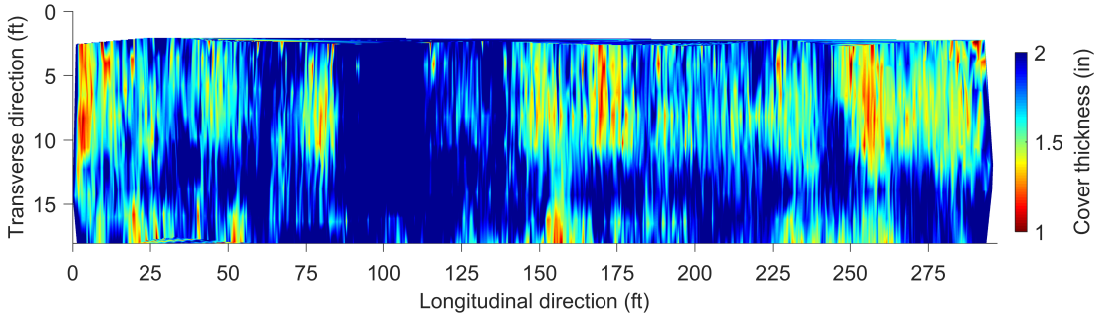

(d)

Fig. 4.13. GPR maps of bridge deck S006 29351 (a) amplitude, (b) velocity, (c) direct-coupling, and (d) cover thickness. (Not to scale).

4.3 Bridge deck 2 - ID: S077 05693R

Bridge S07705693R was tested in the afternoon of August 1, 2018 in Lincoln, Nebraska. The satellite image of the bridge is shown in the **Figure 4.14**. The bridge deck is 180.1 ft. long with two lanes and carry one way traffic. The bridge deck has a concrete overlay. Due to time constraints at the time of testing, only the northbound lane and the wide shoulder of the bridge deck was tested. Four nondestructive testing techniques were deployed on the bridge deck. Vertical Electrical Impedance, Ground Penetrating Radar, Acoustic sensing, and high definition imaging. The NDE test results are presented in the following subsections.

Fig. 4.14. Google map picture of the bridge S077 05693R (map data ©2018 Google)

Impedance

The results of the vertical impedance scanning of Bridge Deck 2 are shown in **Figure 4.15**. To evaluate Bridge Deck 2 with the VEI scanner, both the right lane and right shoulder were scanned twice. During the four passes across the bridge deck, 12.0, 10.8, 11.6, and 10.2 gallons of water were applied to the deck surface. These amounts corresponded to approximately 0.004 to 0.005 gallons per square foot. Like Bridge Deck 1, Bridge Deck 2 had consistent transverse lines characterized by low impedance across the bridge deck; however, the lines are less frequent and less distinct than those observed on Bridge Deck 1. Nebraska Bridge Deck 2 also had a longitudinal line characterized by low impedance approximately 10 ft from the parapet wall. This line corresponded to a construction joint present on the bridge directly beneath the shoulder line. The GPR map often detected these defects when transverse lines intersected the longitudinal line. The other main feature of the impedance map for Bridge Deck 2 is the occurrence of multiple large areas of low impedance near both ends of the bridge. These locations correlate very well with the GPR

data. Although these areas exhibited no visually apparent defects, a chain drag indicated that these locations were delaminated. Lastly, areas along the shoulders of the deck in which debris had accumulated also correlated spatially with some of the low-impedance areas on the map; these areas may have been more susceptible to salt accumulation during winter. The impedance values changed slightly between the first and second passes; however, the impedance values did not change significantly between the second and third passes. For this bridge deck, the low-impedance chloride concentration sampling location was positioned at a longitudinal distance of 176 ft and a transverse distance of 16 ft, while the high-impedance chloride concentration sampling location was positioned at a longitudinal distance of 102 ft and a transverse distance of 12 ft. The results of the chloride concentration testing are shown in **Table 4.1**.

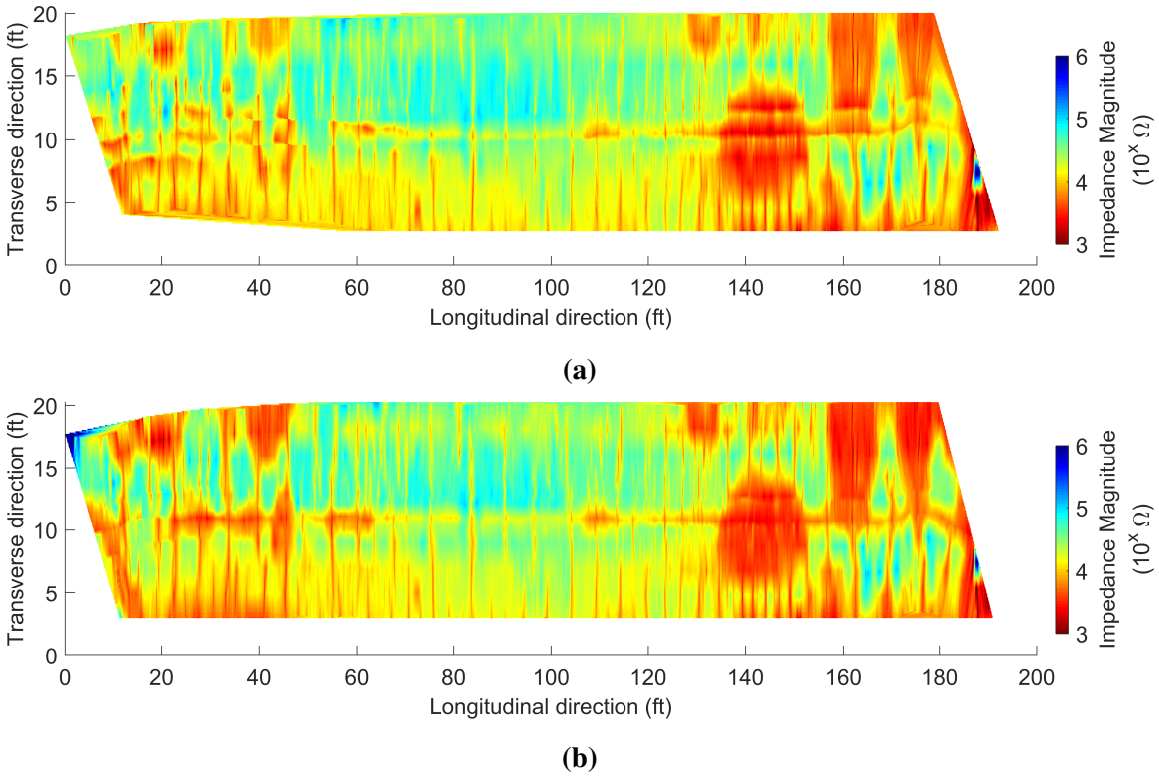

Fig. 4.15. VEI map of Bridge Deck S077 05693R generated from the first pass (a) and second pass (b). (Not to scale).

Acoustic

The acoustic system scanned this bridge with 6 ft. coverage width and used 3 scans to cover the north bound on this bridge. **Figure 4.16** shows the delamination map of the bridge deck. Acoustic images shows a major delamination around 30 ft. in longitudinal direction from the origin. High traffic flow on this bridge caused high noise level which is shown as light blue spots on the map.

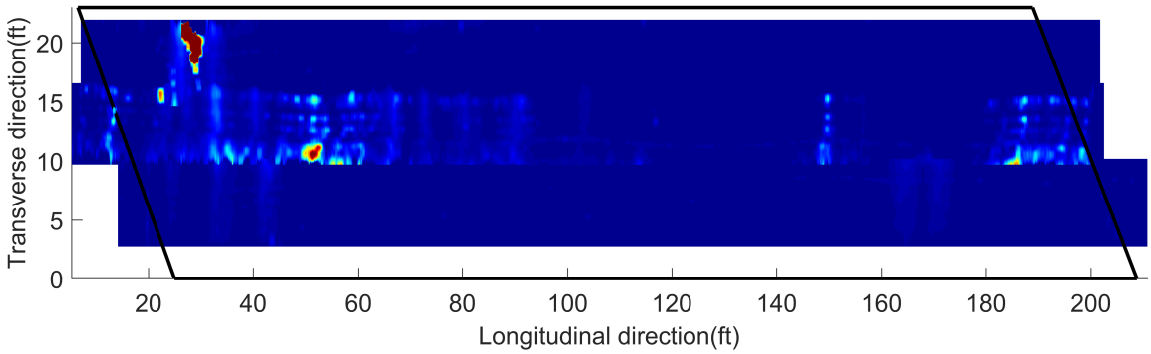

Fig. 4.16. Delamination map of Bridge Deck S07705693R. (Not to scale).

GPR

A GSSI SIR-4000 GPR systems with 1.5 GHz antenna was used to test northbound lane and shoulder of this bridge. The line spacing between scan paths were 2 ft and 10 scans were recorded along the direction of traffic. For this bridge, the positions of the rebars were calculated using a GPS device mounted on the survey cart. From GPR data collected on this bridge, direct coupling amplitude, velocity, depth-corrected amplitude, and cover thickness map are generated. **Figure 4.17a** shows the depth-corrected amplitude map of the bride deck. Low amplitudes of the rebar reflections indicate high attenuation of the signal. High attenuation from southern joint until 50 ft. and from 125 ft to the northern joint of the bridge in longitudinal direction indicate severe deterioration in the bridge deck. High signal attenuation can also be observed along the bridge joints. **Figure 4.17b** shows the wave velocity map of bridge deck. Low wave velocity around 135 ft. to 150 ft. matches with high attenuation on the **Figure 4.17a**. The low direct coupling amplitude region in the **Figure 4.17c** also agrees with high attenuation regions on the **Figure 4.17a**. **Figure 4.17d** shows the cover thickness map of the bridge deck. Because this bridge deck has a concrete overlay, the total cover thickness is larger than 4 inch in most areas.

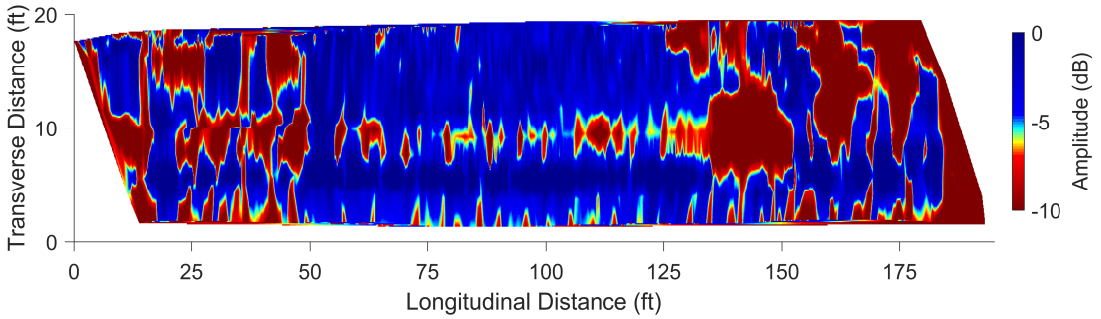

(a)

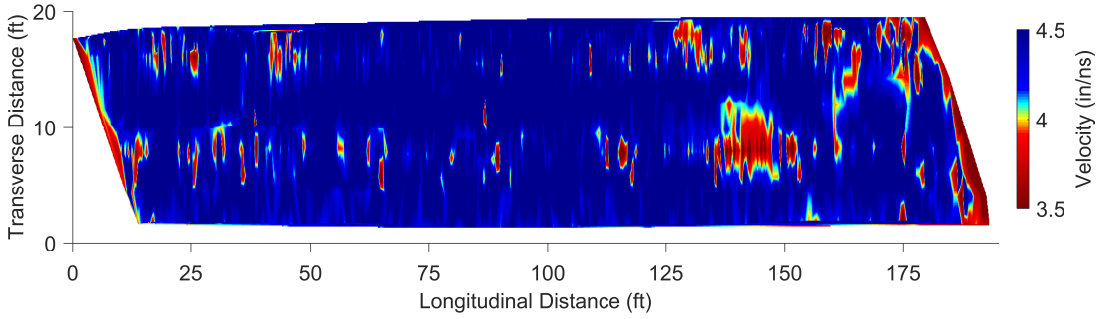

(b)

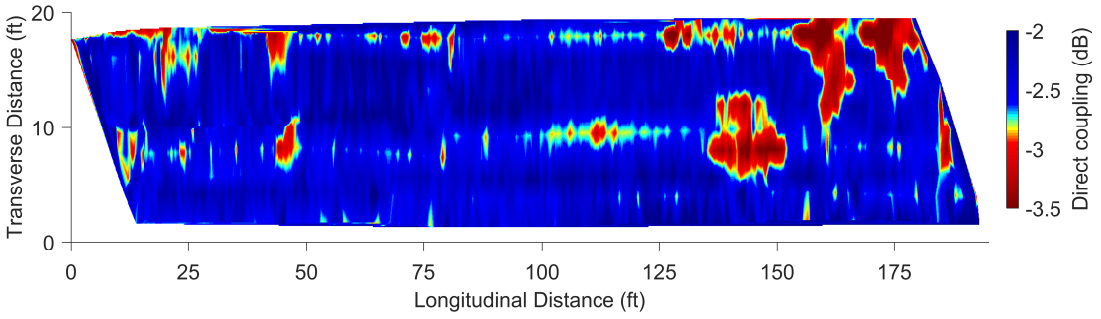

(c)

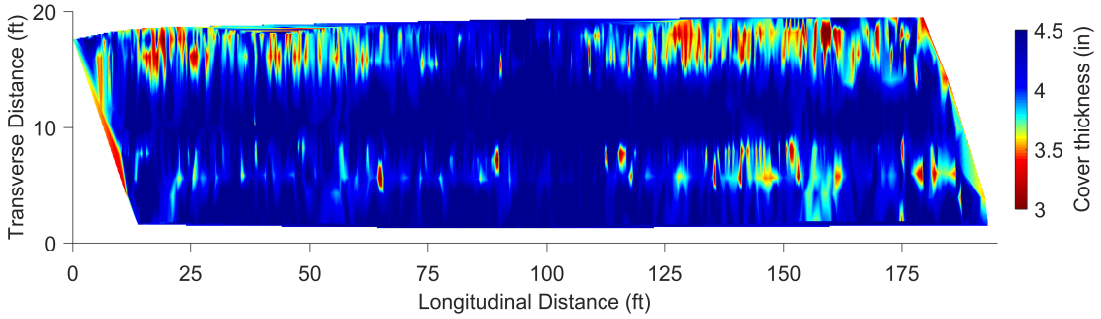

(d)

Fig. 4.17. GPR maps of bridge deck S077 05693R (a) amplitude, (b) velocity, (c) direct-coupling, and (d) cover thickness. (Not to scale).

High resolution images

We obtained 8 sequences along the longitudinal direction of the bridge. Each sequence consists of about 140 frames and each frame has four images from the four cameras. The resolution of each image is 2448 by 2048 pixel. The acquisition speed was approximately 20 miles per hour and the frame rate was set to 25 frames per second. **Figure 4.18** shows some examples of the collected images.

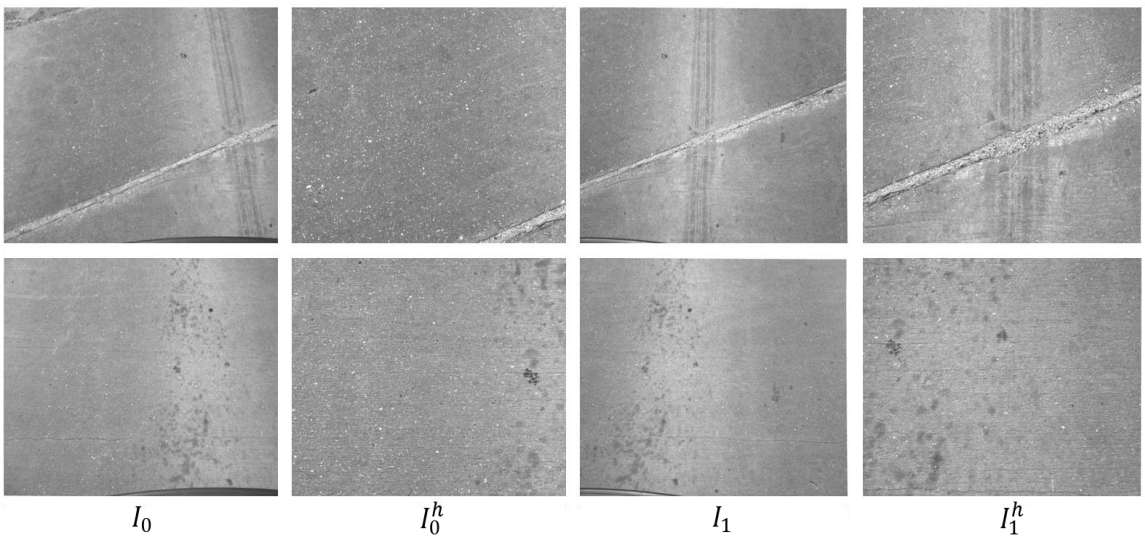

Fig. 4.18. Images collected through our multi-view camera system. Each row represents one frame with four images and consists of two wide field of view images, I_0 and I_1, and two high-resolution images I_0^h and I_1^h.

We implemented the localization and crack detection tasks described earlier. For the localization and 3D mapping, we implemented our own system based on ORB-SLAM which takes a single-view sequence of images and performs simultaneous localization and mapping. Our system uses the ORB features and Bag-of-Words representation [37] and selects key-frames (which are a subset of a sequence) for localization and mapping. It detects loops and corrects any accumulated error along the loops. Our implementation takes multiple sequences of multi-view frames. We calibrated the four cameras in which two of them have wide-angle views with overlapping images. We implemented stereo reconstruction and utilized the results for mapping and optimizing the estimated pose as described earlier in the test procedures. For each view, we extracted ORB features and generated its corresponding Bag-of-Words vector using DBoW2 [37]. With this image-level

descriptor, we generated a graph by applying the proposed sequence matching strategy. The graph is traversed in breadth first order but we employed a priority queue to visit the closest frame from the center of the bridge first, among all immediate neighbors of the visited frames. **Figure 4.19** shows the reconstructed camera poses and 3D points and **Figure 4.20** shows the global map of the high-resolution images stitched together. The size of one pixel in the stitched map is 10 mils (0.25 mm). **Figure 4.21** shows the global map of detected transverse cracks.

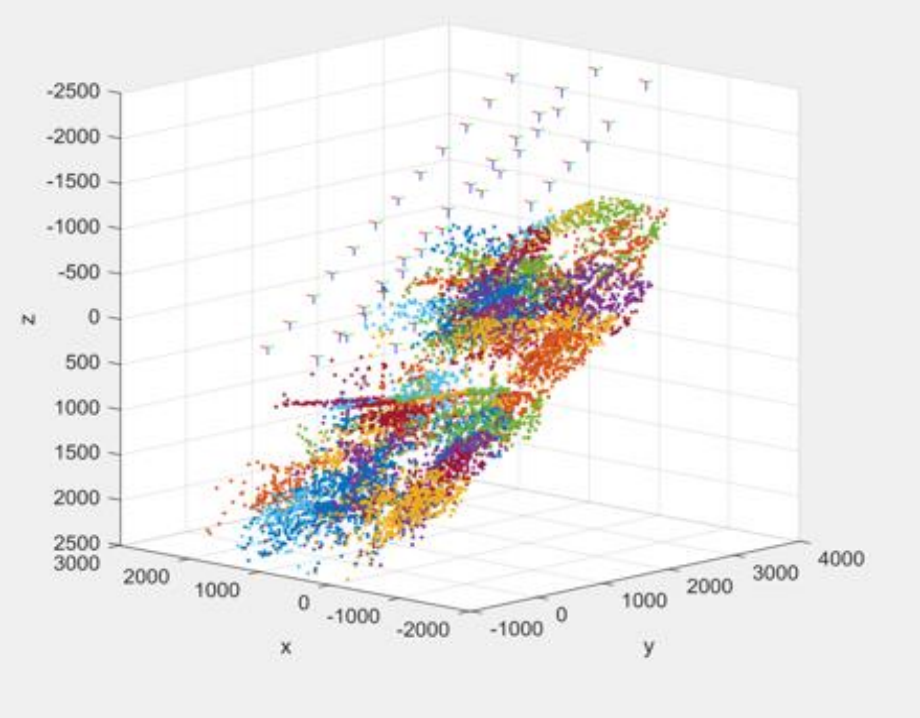

Fig. 4.19. The reconstructed camera pose of all sequences and reconstructed 3D points.

After stitching all images to construct a global map, we implemented the crack detection method introduced in the test procedures section. To detect the crack pixels, we did not examine all pixels but we checked one pixel that has a minimum intensity in each patch generated by a regular grid. A 5 by 5 patch was used in this experiment. **Figure 4.22** and **Figure 4.23** show an example of the detected cracks.

As mentioned earlier, these transverse cracks caused by restrained shrinkage is the main path where chlorides (from deicing salt) penetrate through and corrode the top and bottom of steel reinforcement. This will eventually be the reason why bridge decks deteriorate.

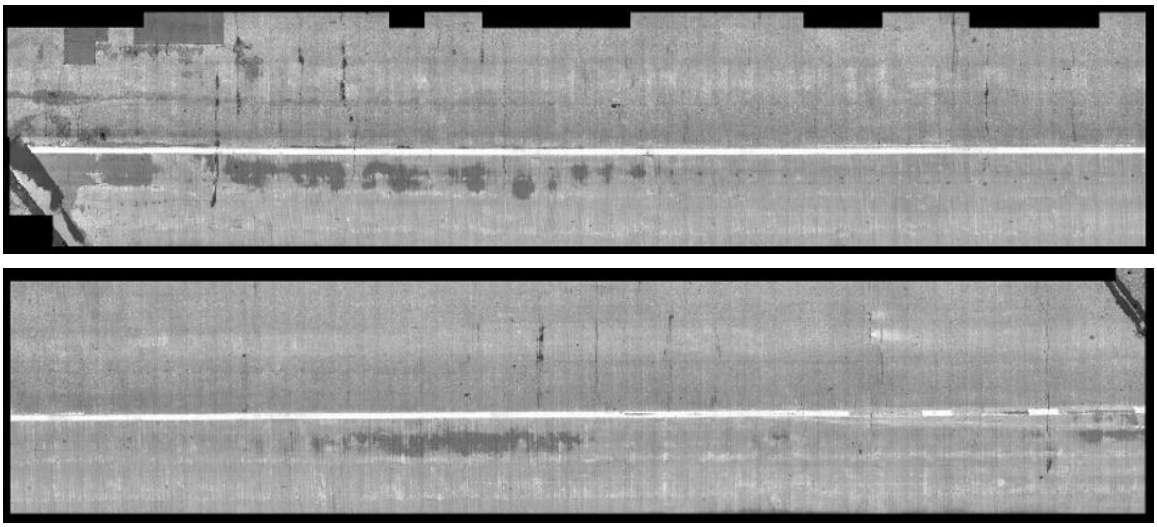

Fig. 4.20. Global map with stitched images of the top surface of an entire bridge deck.

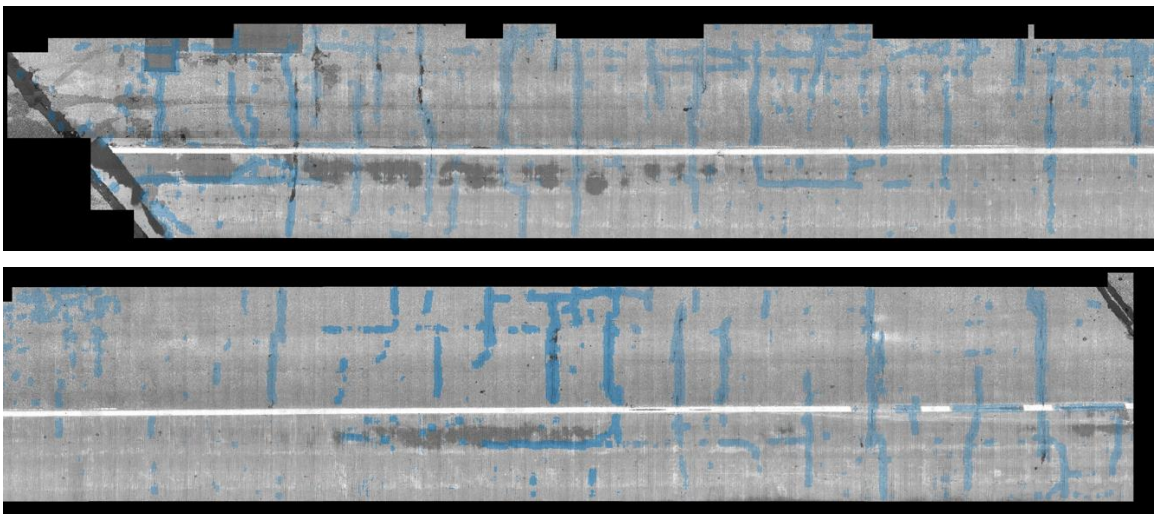

Fig. 4.21. Global map of detected cracks on the top surface of the entire bridge deck.

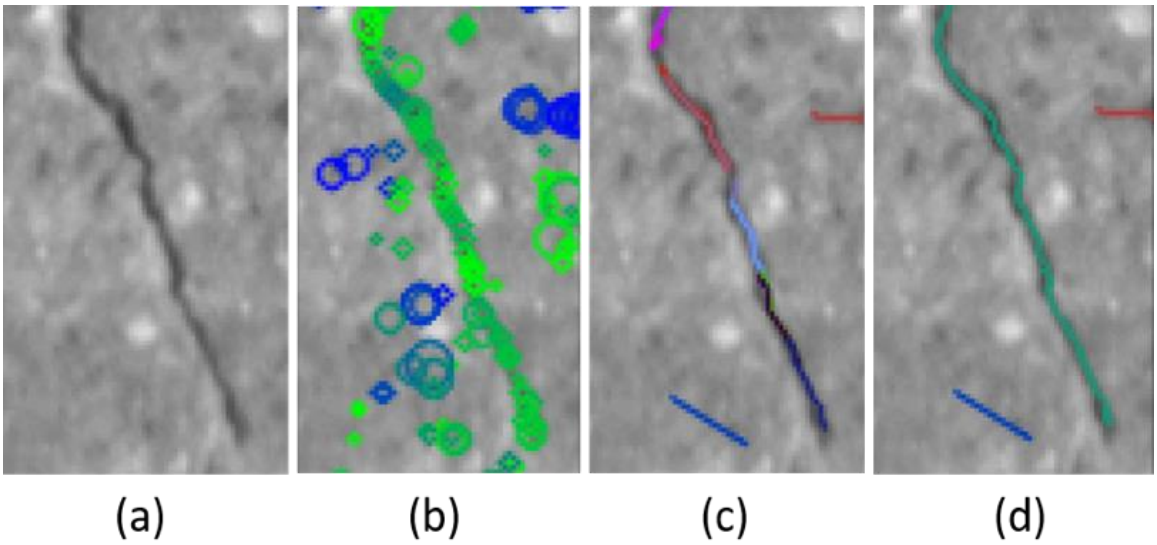

Fig. 4.22. Detected crack-pixels and generated crack-segments: (a) input image, (b) detected crack-pixels: blue colored circles represent crack-pixels in a different direction than the green colored circles of crack-pixels in one dominating orientation. The size of circle represents scale of the crack-pixel, (c) represents initialized and extended crack-segments and (d) represents linked crack-segments.

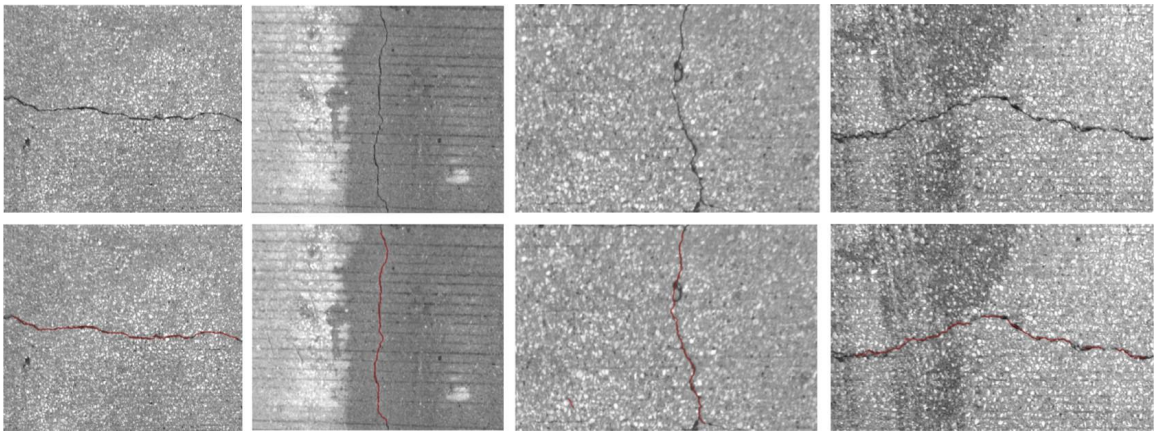

Fig. 4.23. Cracks detected on the top surface of a bridge deck.

4.4 Bridge deck 3 - ID: S015 01730

NDT survey on bridge S07705693R was conducted in the morning of August 2, 2018 in Fairbury, Nebraska. The satellite image of the bridge is shown in the **Figure 4.24**. The asphalt overlaid bridge deck is 54.1 ft. long with two lanes and carries two-way traffic. Since the asphalt overlay covers the bridge deck surface, high resolution imaging and acoustic scanning were not possible for this bridge deck. Therefore, only GPR and VEI were used to survey this bridge deck.

Fig. 4.24. Google map picture of the bridge S015 01730 (map data ©2018 Google)

Impedance

The results of the vertical impedance scanning of Bridge Deck 3 are shown in **Figure 4.25**. To evaluate Bridge Deck 3 with the VEI scanner, both the northbound and southbound lanes were scanned three times. During the six passes across the bridge deck, 14.2, 8.1, 6.7, 14.1, 9.8, and 11.5 gallons of water were applied to the deck surface. These amounts corresponded to approximately 0.008 to 0.017 gallons per square foot for the six passes, which was above the recommended water usage specification. The extra water was deliberately applied, however, to ensure that the asphalt overlay was sufficiently soaked for testing. Noticeably, there are lower impedance values along both edges of the bridge and down the center. The lower impedance values along the edge of the bridge are possibly the result of snow storage and salt accumulation during winter. The lower impedance values down the middle are likely caused by a cold joint during the asphalt placement process.

Another prominent feature shown in this bridge map is the slightly lower impedance line that runs diagonally from location (20 ft, 20 ft) to (33 ft, 3 ft). Because the impedance

data were able to be quickly processed on site, a preliminary scanning map was obtained after the first pass. To investigate this diagonal line, the bridge engineers participating in the work inspected the bottom of the bridge deck. They determined that the line coincided with a visible crack in the asphalt overlay that was caused from an underlying construction joint, which exhibited efflorescence on the underside of the bridge. The impedance map revealed this defect that otherwise would not have been observed. Finally, there is a line of lower impedance visible in the upper lane of the map. Although there was no physical evidence of defects along the line, it coincided with a wheel path, where deterioration is probably more accelerated compared to the rest of the bridge deck. For this bridge deck, the low-impedance chloride concentration sampling location was positioned at a longitudinal distance of 43 ft and a transverse distance of 11 ft, while the high-impedance chloride concentration sampling location was positioned at a longitudinal distance of 25 ft and a transverse distance of 9 ft.

GPR

A GSSI SIR-4000 GPR systems with 1.5 GHz antenna was used to test entire surface area of this bridge. The spacing between scan paths were 1 ft and 25 scans were recorded along the direction of traffic. Since the bridge is relatively short, for this bridge, the positions of the rebars were calculated using cart encoder.

After post-processing of the GPR data, we found that the rebar reflections cannot be clearly identified because of very thick asphalt overlay. **Figure 4.26** shows an example of GPR B-scan image recorded on the bridge deck. Therefore, only the direct coupling amplitude map could be generated.

Figure 4.27 shows the direct coupling amplitude map of the asphalt surface. It is interesting to notice the GPR surface reflection amplitude maps agrees with the VEI map well. The GPR map shows deterioration along both joints and along the edge of the south bound lane. The low amplitude regions in the south bound lane are probably along the wheel path. Similar to the VEI map, the GPR image shows two diagonal low amplitude lines. Comparing the VEI and GPR images, we found the GPR image seems to have better spatial resolution in the transverse direction.

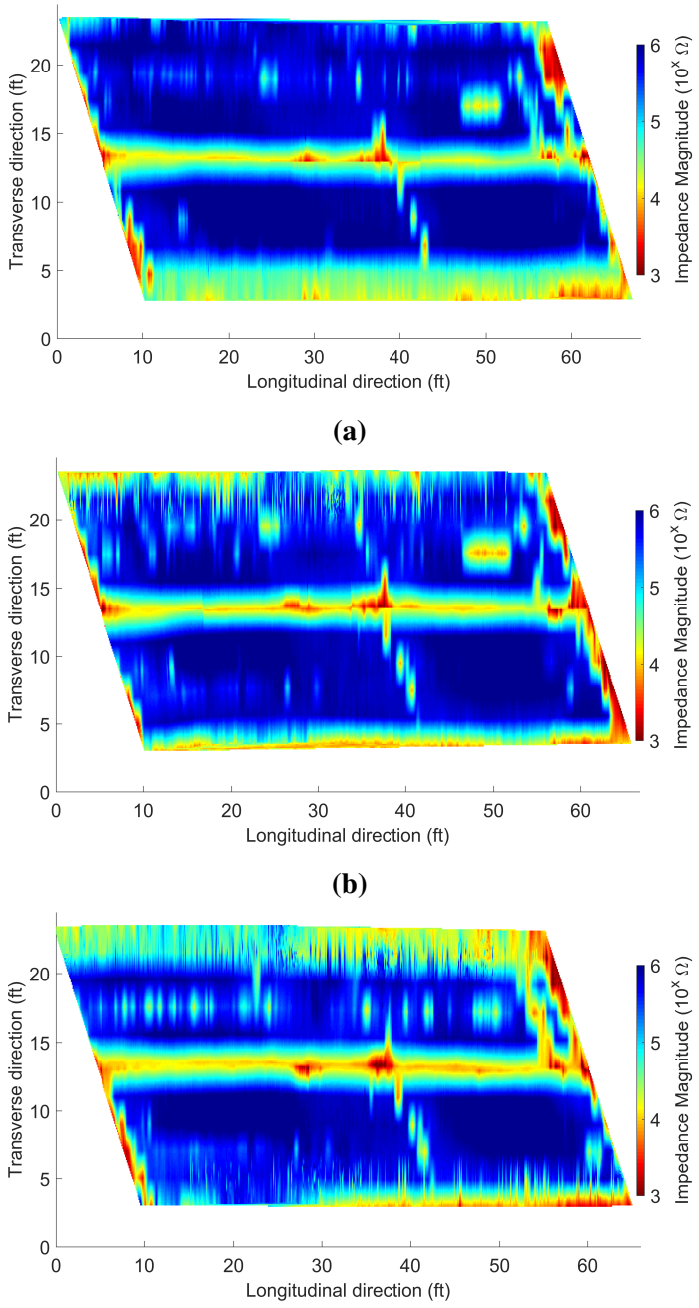

(a)

(b)

(c)

Fig. 4.25. VEI map of bridge deck S015 01730 generated from the (a) first pass. (b) second pass. (c) third pass. (Not to scale).

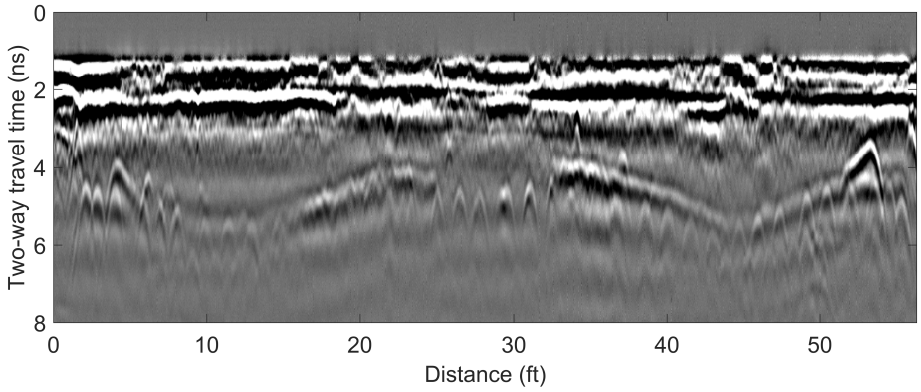

Fig. 4.26. B-scan image recorded on the bridge deck S015 01730

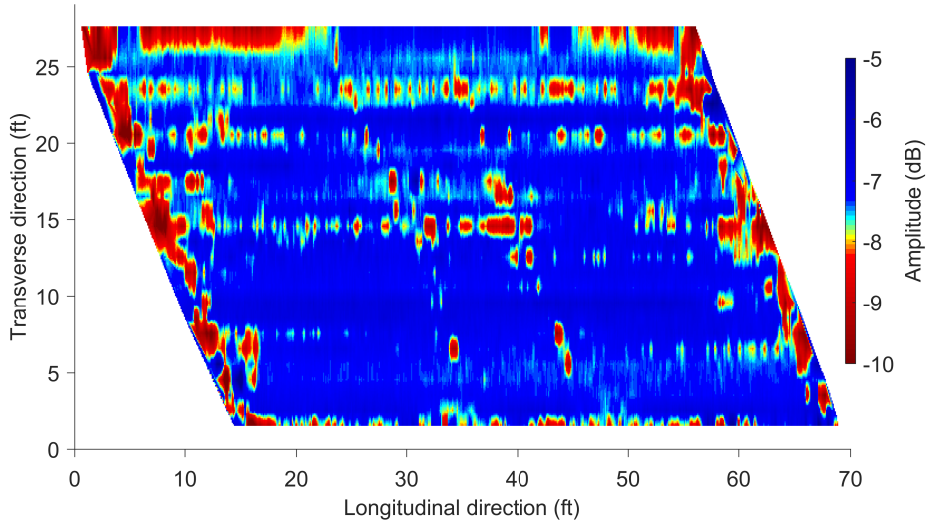

Fig. 4.27. Direct coupling amplitude map of bridge deck S015 01730. (Not to scale).

4.5 Chloride concentration

Chloride concentration test provides ground-truth regarding the NDT measurements. The results of the chloride concentration testing are shown in **Table 4.1**. For each of the three Nebraska bridge decks, the chloride concentrations measured at the high-impedance location were lower than those measured at the low-impedance location, as expected. GPR amplitude also has a low value at the chloride test locations where chloride concentration is high.

Table 4.1. Chloride Concentration Test Results

Bridge Deck ID	Longit. Dist. (ft)	Trans. Dist. (ft)	Average Depth (in)	Chloride. Conc. *	VEI (Ω)	GPR Amp. (dB)
S006 29351	162	9	0.5	17.4	32,000	-3.65
			1.5	2.0		
	212	15	0.5	20.0	10,000	-8.87
			1.5	10.6		
S077 05693R	102	12	0.5	4.0	79,000	-3.1
			1.5	1.1		
	176	15.5	0.5	13.3	2,500	-13.8
			1.5	9.0		
S015 01730	24.5	8.5	0.5	10.4	630,000	-6.71**
			1.5	8.6		
	42.5	10.5	0.5	13.9	6,300	-8.28**
			1.5	13.4		

*(lb Cl^{-}/yd^{3} Concrete)

** Direct coupling amplitude

Chapter 5

Data Analysis

Four NDT technologies were demonstrated on three bridges in this project. On the second bridge, S077 05693R, we were able to successfully collect and analyze data using all these NDT technologies. In this section, we focus on the data analysis of this bridge and perform data fusion. For the analysis, we choose the VEI data collected during the second pass (**Figure 4.15b**), depth-corrected amplitude map from GPR data (**Figure 4.17a**), delamination map of acoustic scanning system (**Figure 4.16**), and detected cracks on the top surface of the bridge deck from the high definition images (**Figure 4.21**).

5.1 NDE data comparison

Exposure of reinforced concrete to chloride due to use of deicing salt is a major cause of rebar corrosion. Such exposure increases the electrical conductivity of concrete and reduces its resistivity. Dissipation of EM wave energy in a dielectric medium increases with conductivity. Thus, GPR signal attenuation in deteriorated areas of bridge deck is higher than intact regions. On the other hand, electrical impedance of concrete reflects the difficulty with which current can flow through it when an alternating electrical potential is applied. Therefore, GPR and VEI both measure the variation of concrete resistivity or conductivity. **Figure 5.1** shows the overlapped GPR depth-corrected amplitude, VEI, and acoustic maps. Comparing the marked areas by two methods verifies that GPR and VEI evaluate the reinforced concrete based on the same principle.

The black areas on the map shows the major delaminations detected by acoustic scanning system. Although, location of delaminations agree with the VEI and GPR deteriorated areas, only a few area of delamination were detected by the acoustic method. It is unclear if the

high traffic noise affected the acoustic scanning system or the bridge deck did not have many shallow delaminations even though deterioration was detected by GPR and VEI methods.

In the **Figure 5.2** location of surface cracks are plotted on the GPR rebar amplitude map. The surface crack locations agree with the low GPR amplitude regions except for the region from 70 ft to 120 ft in longitudinal direction. Transverse cracks are direct pathways for chloride ions from surface to rebars which causes increase in concrete conductivity. Large portion of bridge deck with low rebars amplitude (0-50 ft, 130-180 ft) matches well with location of transverse cracks. In **Figure 5.3** the surface cracks are plotted on the VEI map. Similar to the comparison with GPR map, locations of the transverse cracks agree well with areas of low concrete impedance in the range of 0 to 50 ft. and 130 to 180 ft. These comparison results indicate that the surface imaging and crack quantification methods are effective methods for fast screening of concrete bridge decks.

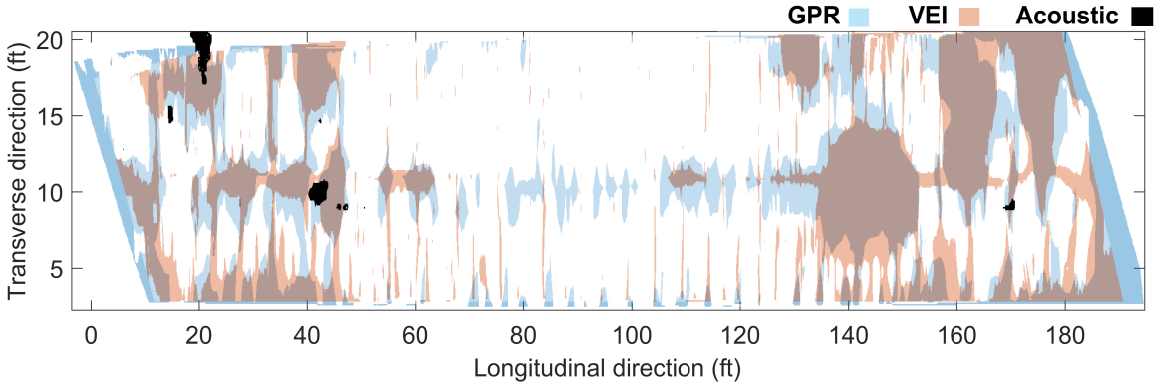

Fig. 5.1. GPR, VEI, and acoustic maps overlapped for bridge deck S077 05693R.

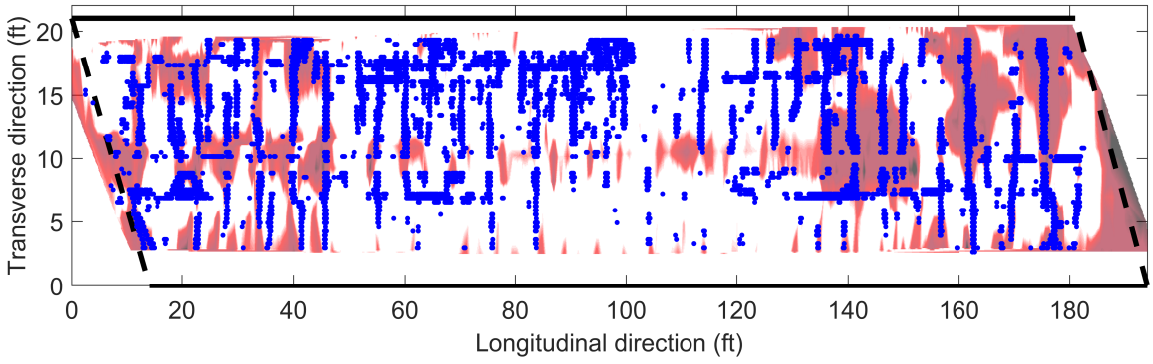

Fig. 5.2. GPR map and crack locations for bridge deck S077 05693R.

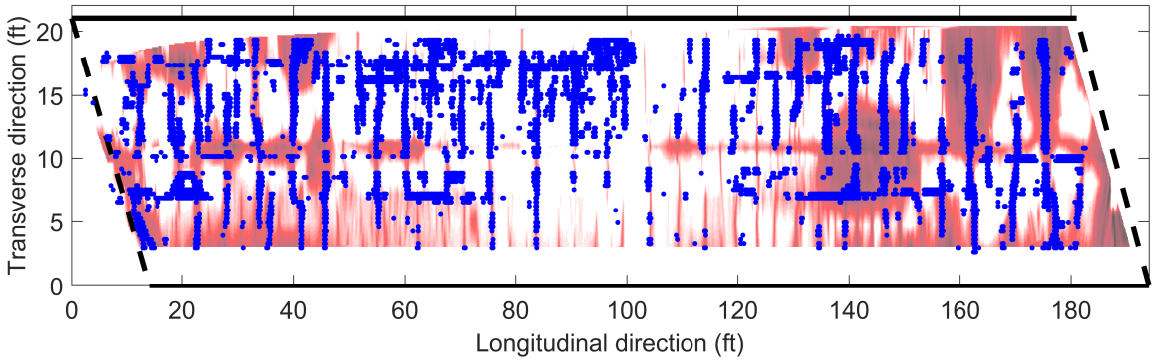

Fig. 5.3. VEI map and crack locations for bridge deck S077 05693R.

5.2 Data fusion

In the **Comparison** section, we attempted to graphically show the result of GPR, VEI, and acoustic on the same plot. This approach may provide intuitive information about the deteriorated regions of bridge deck, but does not give the quantitative information about the total deteriorated area. In addition, VEI, GPR, and acoustic data have distinct values and plotting all data on the same plot requires variable transformation. Thus, we need to combine the data from three sources into a comprehensive dataset which can represent all NDT results.

In general, the mechanism of integrating the processed data and related information from multiple sensors is called information fusion. These methods are used to improve accuracy and inferences which could not be done by utilizing a single sensor [38]. With the fused data, we can calculate total deteriorated area by setting a threshold on the fused dataset. Many approaches have been proposed in the literature in order to integrate the multi-source data [39–41]. Herein two data fusion algorithms are briefly explained and implemented on the available data. The results from each method are presented and their advantages are discussed.

Principle Component based data fusion

One way of integrating the GPR, VEI, and acoustic measurements is to calculate the linear combination of standardized value from all sensors (see equation 5.1). In Equation 5.1, the sensor values are normalized by their standard deviation to prevent domination of one sensor results over others, and the coefficients ϕ_1, ϕ_2, and ϕ_3 are the weights correspond

to each measurement. These coefficients have to be chosen in a way that maximizes the variation on the A_{fused} vector, so that most source features are kept in the fused image. Thus the three dimension data are transformed to a single variable, A_{fused}, that indicates the concrete condition.

$$A_{fused} = \phi_1\left(\frac{A_{GPR}}{\sigma_{GPR}}\right) + \phi_2\left(\frac{A_{VEI}}{\sigma_{VEI}}\right) + \phi_3\left(\frac{A_{acoustic}}{\sigma_{acoustic}}\right) \tag{5.1}$$

The weights ϕ_1, ϕ_2, and ϕ_3 can be calculated using Principle Component Analysis (PCA) method. PCA is a statistical technique that can be used to determine the standardized linear projection coefficients, which maximizes the variance in the projected space [42]. Coefficients of the first principle component, $\phi_1 = 0.7066$, $\phi_2 = 0.7070$, and $\phi_3 = -0.0305$ show the contribution of each NDT method to the fused result. **Figure 5.4** shows the fused deterioration map of the bridge S077 05693R. The fused map looks similar to VEI and GPR because of large coefficients, ϕ_1 and ϕ_2. Location of delaminations detected by acoustic method are marked on the fused map. Those delaminations which do not agree with VEI and GPR are masked.

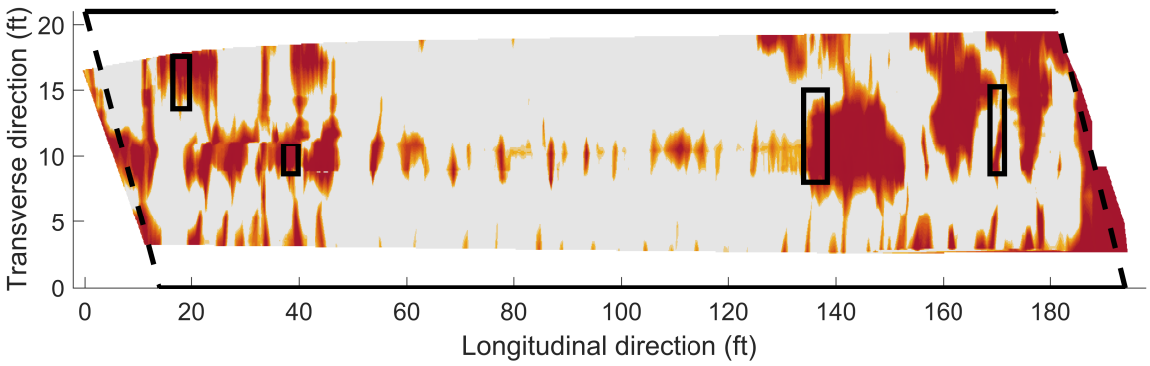

Fig. 5.4. Fused deterioration map of the bridge S077 05693R using PCA method.

Wavelet-based image fusion

Discrete Wavelet Transformation (DWT) is a mathematical transformation which is widely used in image processing to decompose an image into specific wavelet coefficients to eliminate noise, extract features, and multi-source image fusion [43, 44]. Through a fusion rule, the complex wavelet coefficients from all images are mixed and final wavelet coefficients of fused image are obtained. The final step is to take inverse wavelet transform from mixed wavelet coefficients to achieve the fused image. The advantage of this method is that in the fused image, most of the features of the input images are kept. The pipeline of

the wavelet-based image fusion is shown in the **Figure 5.5**. **Figure 5.6** shows the fused map from VEI, GPR, and acoustic method. The location of delaminations detected by acoustic scanning system are marked with rectangles on the map. Unlike PCA method, acoustic method results are visible on this map.

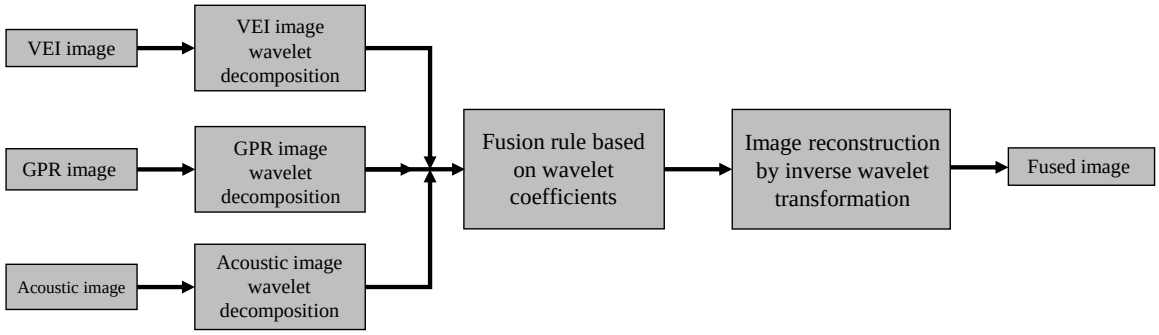

Fig. 5.5. Flowchart of wavelet-based image fusion algorithm.

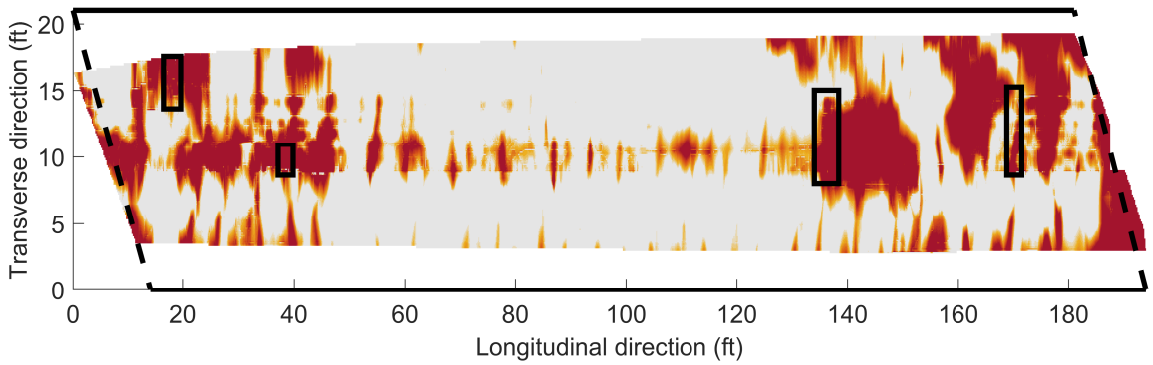

Fig. 5.6. Fused deterioration map of the bridge S077 05693R using wavelet-based image fusion method.

Chapter 6

Conclusions

A moving NDE platform was developed and implemented for bridge deck inspection. Field demonstration of the platform with the VEI measurement system showed that the system is able to provide accurate positions using the localization box. Along with the NDE platform equipped with the VEI system, three other NDE technologies were demonstrated on three Nebraska bridges with different bridge deck overlays: bare concrete, concrete overlay, and asphalt overlay. All these NDE tests have automated positioning systems. For each bridge, all NDE test results are shown as images to map the deterioration regions on the bridge decks. Different NDE data from all sources are compared and fused to integrate the results for more accurate information about the bridge and to reduce the noise in the data.

The main findings and conclusions of this research project are summarized as follows:

- An NDE platform was developed by the BYU team with low-cost, automated positioning system to synchronize NDE data acquisition and positioning data. The NDE system equipped with vertical electrical impedance (VEI) system was successfully demonstrated on three Nebraska bridges.
- The open structure of the NDE platform will allow connection of other NDE test systems, such as the acoustic scanning system, if the NDE test system has an open data connector. The GSSI GPR system uses proprietary software, and we could not directly connect the GPR system to the NDE platform.
- The GPR and VEI test results show high level of similarity because both methods measure the electrical properties of reinforced concrete. The GPR may have a better spatial resolution in the longitudinal direction. The lateral resolution depends on the line spacing used in the survey.
- Transverse cracks are the direct paths for water and chloride to reach rebars. By comparing the GPR and VEI maps with the HD images, we found that the locations

of transverse cracks match with the high conductivity regions of the bridge deck. However, GPR and VEI images do not show deterioration in scattered surface cracks. Further information about crack dimensions and crack width is needed to verify if these scattered cracks may not cause deterioration to the reinforced concrete.

- By comparing GPR and VEI maps with chloride concentration results on the asphalt overlaid bridge deck, we found that the GPR direct coupling map provides reliable information about the condition of the asphalt overlay. In cases where GPR signal attenuation is high and most of the rebar reflections are lost, the direct coupling map can be used for bridge deck evaluation.
- PCA based data fusion gives three principle components in which the first principle component has the highest variation. Since this method is based on the linear combination of sensors' measurements, noisy values from sensors with uncorrelated data with others will be suppressed. That is why acoustic results are not visible in the fused image.
- Wavelet based image fusion method maps the features from all NDT results into a final image. Rationale for the fusion rule is to keep all information from sources. This method is suitable for situations where we are certain that all sensors work properly despite their difference in their output.
- Chloride concentration test provides ground-truth data for the NDT tests. The measured chloride concentration of concrete suggests that GPR and VEI provide reliable results for evaluating the bridge deck condition.

Bibliography

[1] The American Road & Transportation Builders Association, "2019 Bridge Report," ARTBA, Washington DC, 2019.

[2] C. Andrade and C. Alonso, "Test methods for on-site corrosion rate measurement of steel reinforcement in concrete by means of the polarization resistance method," *Materials and Structures*, vol. 37, pp. 623–643, Nov 2004.

[3] ASTM D4580-12, "Standard practice for measuring delaminations in concrete bridge decks by sounding," West Conshohocken, PA: American Society for Testing and Materials, 2018.

[4] ASTM C876-15, "Standard test method for corrosion potentials of uncoated reinforcing steel in concrete," West Conshohocken, PA: American Society for Testing and Materials, 2016.

[5] N. Gucunski, A. Imani, F. Romero, S. Nazarian, D. Yuan, H. Wiggenhauser, P. Shokouhi, A. Taffe, and D. Kutrubes, *Nondestructive Testing to Identify Concrete Bridge Deck Deterioration*. Washington, DC: The National Academies Press, 2012.

[6] N. Gucunski and S. Nazarian, *Material Characterization and Condition Assessment of Reinforced Concrete Bridge Decks by Complementary NDE Technologies*, pp. 429–439.

[7] W. S. Guthrie, J. L. Larsen, J. S. Baxter, and B. A. Mazzeo, "Automated air-coupled impact-echo testing of a concrete bridge deck from a continuously moving platform," *Journal of Nondestructive Evaluation*, vol. 38, p. 32, Mar 2019.

[8] T. W. Robison and J. E. Tanner, "Bridge deck evaluation using non-destructive test methods," Final Report FHWA-WY-10/07F, Wyoming Department of Transportation, 2011.

[9] J. Tanesi, A. Ardani, *et al.*, "Surface resistivity test evaluation as an indicator of the chloride permeability of concrete.," Final Report FHWA-HRT-13-024, 2012.

[10] H. Sun, S. Pashoutani, and J. Zhu, "Nondestructive evaluation of concrete bridge decks with automated acoustic scanning system and ground penetrating radar," *Sensors*, vol. 18, no. 6, p. 1955, 2018.

[11] H. M. La, R. S. Lim, B. Basily, N. Gucunski, J. Yi, A. Maher, F. A. Romero, and H. Parvardeh, "Autonomous robotic system for high-efficiency non-destructive bridge deck inspection and evaluation," in *2013 IEEE International Conference on Automation Science and Engineering (CASE)*, pp. 1053–1058, Aug 2013.

[12] P. D. Bartholomew, W. S. Guthrie, and B. A. Mazzeo, "Vertical impedance measurements on concrete bridge decks for assessing susceptibility of reinforcing steel to corrosion," *Review of Scientific Instruments*, vol. 83, no. 8, p. 85104, 2012.

[13] B. A. Mazzeo and W. S. Guthrie, "Vertical electrical impedance scanner for concrete bridge deck assessment without direct rebar attachment," Final Report NCHRP IDEA Project 202, 2019.

[14] W. S. Guthrie and B. A. Mazzeo, "Vertical impedance testing for assessing protection from chloride-based deicing salts provided by an asphalt overlay system on a concrete bridge deck," in *Cold Regions Engineering 2015*, pp. 358–369.

[15] Bentley Systems, "Reality modeling software." https://www.bentley.com/en/products/brands/contextcapture, 2019.

[16] N. Gucunski, S.-H. Kee, H. La, B. Basily, A. Maher, and H. Ghasemi, *Implementation of a Fully Autonomous Platform for Assessment of Concrete Bridge Decks RABIT*, pp. 367–378.

[17] H. Sun, J. Zhu, and S. Ham, "Acoustic evaluation of concrete delaminations using ball-chain impact excitation," *The Journal of the Acoustical Society of America*, vol. 141, no. 5, pp. EL477–EL481, 2017.

[18] J. Barton, J. Baxter, W. S. Guthrie, and B. A. Mazzeo, "Large-area electrode design for vertical electrical impedance scanning of concrete bridge decks," *Review of Scientific Instruments*, vol. 90, no. 2, p. 025101, 2019.

[19] J. S. Baxter, W. S. Guthrie, T. Waters, J. D. Barton, and B. A. Mazzeo, "Vertical electrical impedance evaluation of asphalt overlays on concrete bridge decks," *AIP Conference Proceedings*, vol. 1949, no. 1, p. 030011, 2018.

[20] W. S. Guthrie, J. S. Baxter, and B. A. Mazzeo, "Vertical electrical impedance testing of a concrete bridge deck using a rolling probe," *NDT & E International*, vol. 95, pp. 65 – 71, 2018.

[21] H. M. Argyle, "Sensitivity of electrochemical impedance spectroscopy measurements to concrete bridge deck properties," 2014.

[22] Ublox, "NEO-7P u-blox 7 Precise Point Positioning GNSS module Data Sheet." https://www.u-blox.com/sites/default/files/products/documents/NEO-7P_DataSheet_%28UBX-13003787%29.pdf, 2014.

[23] S. Pashoutani and J. Zhu, "Condition assessment of concrete bridge deck with asphalt overlay," Final report Nebraska Department of Transportation SPR-P1(17) M065, 2019.

[24] S. Pashoutani and J. Zhu, "Ground penetrating radar data processing for concrete bridge deck evaluation," *Journal of Bridge Engineering*, vol. 25, will appear in 2020.

[25] A. Di Matteo, E. Pettinelli, and E. Slob, "Early-time gpr signal attributes to estimate soil dielectric permittivity: A theoretical study," *IEEE Transactions on Geoscience and Remote Sensing*, vol. 51, pp. 1643–1654, March 2013.

[26] D. Comite, A. Galli, S. E. Lauro, E. Mattei, and E. Pettinelli, "Analysis of gpr early-time signal features for the evaluation of soil permittivity through numerical and experimental surveys," *IEEE Journal of Selected Topics in Applied Earth Observations and Remote Sensing*, vol. 9, pp. 178–187, Jan 2016.

[27] H. Sun, J. Zhu, and S. Ham, "Automated acoustic scanning system for delamination detection in concrete bridge decks," *Journal of Bridge Engineering*, vol. 23, no. 6, p. 04018027, 2018.

[28] P. Prasanna, K. J. Dana, N. Gucunski, B. B. Basily, H. M. La, R. S. Lim, and H. Parvardeh, "Automated crack detection on concrete bridges," *IEEE Transactions on Automation Science and Engineering*, vol. 13, pp. 591–599, April 2016.

[29] C. M. Yeum and S. J. Dyke, "Vision-based automated crack detection for bridge inspection," *Computer-Aided Civil and Infrastructure Engineering*, vol. 30, no. 10, pp. 759–770, 2015.

[30] H. La, N. Gucunski, S. Kee, and L. Nguyen, "Data analysis and visualization for the bridge deck inspection and evaluation robotic system," *Visualization in Engineering*, vol. 3, 12 2015.

[31] T. Yamaguchi and S. Hashimoto, "Fast crack detection method for large-size concrete surface images using percolation-based image processing," *Machine Vision and Applications*, vol. 21, pp. 797–809, 8 2010.

[32] A. Mohan and S. Poobal, "Crack detection using image processing: A critical review and analysis," *Alexandria Engineering Journal*, vol. 57, no. 2, pp. 787 – 798, 2018.

[33] E. Rosten and T. Drummond, "Machine learning for high-speed corner detection," in *Computer Vision – ECCV 2006* (A. Leonardis, H. Bischof, and A. Pinz, eds.), (Berlin, Heidelberg), pp. 430–443, Springer Berlin Heidelberg, 2006.

[34] M. Calonder, V. Lepetit, C. Strecha, and P. Fua, "Brief: Binary robust independent elementary features," in *Computer Vision – ECCV 2010* (K. Daniilidis, P. Maragos, and N. Paragios, eds.), (Berlin, Heidelberg), pp. 778–792, Springer Berlin Heidelberg, 2010.

[35] E. Rublee, V. Rabaud, K. Konolige, and G. Bradski, "Orb: An efficient alternative to sift or surf," in *2011 International Conference on Computer Vision*, pp. 2564–2571, Nov 2011.

[36] D. Galvez-López and J. D. Tardos, "Bags of binary words for fast place recognition in image sequences," *IEEE Transactions on Robotics*, vol. 28, pp. 1188–1197, Oct 2012.

[37] R. Mur-Artal, J. M. M. Montiel, and J. D. Tardós, "ORB-SLAM: A Versatile and Accurate Monocular SLAM System," *IEEE Transactions on Robotics*, vol. 31, pp. 1147–1163, Oct 2015.

[38] D. L. Hall and J. Llinas, "An introduction to multisensor data fusion," *Proceedings of the IEEE*, vol. 85, pp. 6–23, Jan 1997.

[39] O. Rockinger and T. Fechner, "Pixel-level image fusion: the case of image sequences," in *Signal Processing, Sensor Fusion, and Target Recognition VII* (I. Kadar, ed.), vol. 3374, pp. 378 – 388, International Society for Optics and Photonics, SPIE, 1998.

[40] K. C. Rajini and S. Roopa, "A review on recent improved image fusion techniques," in *2017 International Conference on Wireless Communications, Signal Processing and Networking (WiSPNET)*, pp. 149–153, March 2017.

[41] M. Li and Y. Song, "Review on technology of pixel-level image fusion," in *Proceedings of 2013 2nd International Conference on Measurement, Information and Control*, vol. 1, pp. 341–344, Aug 2013.

[42] H. Gao, "A simple multi-sensor data fusion algorithm based on principal component analysis," in *2009 ISECS International Colloquium on Computing, Communication, Control, and Management*, vol. 2, pp. 423–426, Aug 2009.

[43] Hui Li, B. S. Manjunath, and S. K. Mitra, "Multi-sensor image fusion using the wavelet transform," in *Proceedings of 1st International Conference on Image Processing*, vol. 1, pp. 51–55 vol.1, Nov 1994.

[44] X. Xu, Y. Wang, and S. Chen, "Medical image fusion using discrete fractional wavelet transform," *Biomedical Signal Processing and Control*, vol. 27, pp. 103 – 111, 2016.